Efficient pre-mRNA cleavage prevents replication-stress-associated genome instability

Teloni, Federico ; Michelena, Jone ; Lezaja, Aleksandra ; Kilic, Sinan ; Ambrosi, Christina ; Menon, Shruti ; Dobrovolna, Jana ; Imhof, Ralph ; Janscak, Pavel ; Baubec, Tuncay ; Altmeyer, Matthias

Abstract: Cellular mechanisms that safeguard genome integrity are often subverted in cancer. To identify cancer-related genome caretakers, we employed a convergent multi-screening strategy coupled to quantitative image-based cytometry and ranked candidate genes according to multivariate readouts reflecting viability, proliferative capacity, replisome integrity, and DNA damage signaling. This unveiled regulators of replication stress resilience, including components of the pre-mRNA cleavage and polyadenylation complex. We show that deregulation of pre-mRNA cleavage impairs replication fork speed and leads to excessive origin activity, rendering cells highly dependent on ATR function. While excessive formation of RNA:DNA hybrids under these conditions was tightly associated with replication-stress-induced DNA damage, inhibition of transcription rescued fork speed, origin activation, and alleviated replication catastrophe. Uncoupling of pre-mRNA cleavage from co-transcriptional processing and export also protected cells from replication-stress-associated DNA damage, suggesting that pre-mRNA cleavage provides a mechanism to efficiently release nascent transcripts and thereby prevent gene gating-associated genomic instability.

DOI: https://doi.org/10.1016/j.molcel.2018.11.036

Article

Molecular Cell

Efficient Pre-mRNA Cleavage Prevents Replication-Stress-Associated Genome Instability

Graphical Abstract

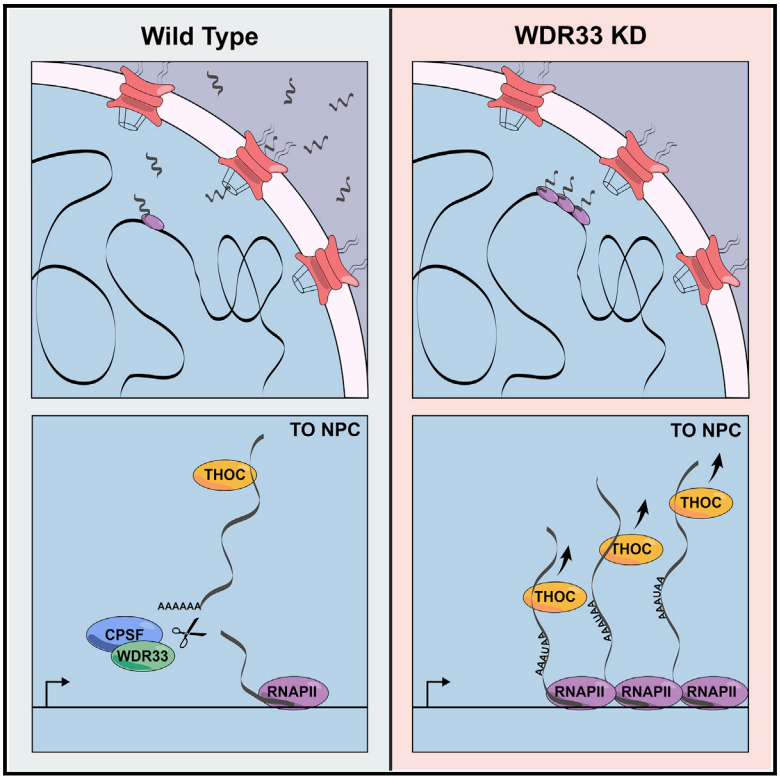

Highlights

- A convergent multi-screening approach reveals modulators of replication stress (RS)
- Efficient WDR33-mediated pre-mRNA cleavage confers RS resilience
- RNA:DNA-hybrid formation occurs upon RS-induced DNA breakage
- THO nuclear export complex drives RS sensitivity of WDR33-depleted cells

Authors

Federico Teloni, Jone Michelena, Aleksandra Lezaja, ..., Pavel Janscak, Tuncay Baubec, Matthias Altmeyer

Correspondence

matthias.altmeyer@uzh.ch

In Brief

Replication stress is a hallmark of many cancers. Teloni et al. identify the pre-mRNA cleavage factor WDR33 as regulator of replication stress resilience and demonstrate that, when WDR33 function is impaired, unreleased nascent transcripts and genomic loci re-localize toward the nuclear periphery, where they cause replication stress and DNA damage.

Teloni et al., 2019, Molecular Cell *73*, 1–14
February 21, 2019
https://doi.org/10.1016/j.molcel.2018.11.036

CellPress

Please cite this article in press as: Teloni et al., Efficient Pre-mRNA Cleavage Prevents Replication-Stress-Associated Genome Instability, Molecular Cell (2018), https://doi.org/10.1016/j.molcel.2018.11.036

Molecular Cell
Article

Efficient Pre-mRNA Cleavage Prevents Replication-Stress-Associated Genome Instability

Federico Teloni,[1,4] Jone Michelena,[1] Aleksandra Lezaja,[1,4] Sinan Kilic,[1] Christina Ambrosi,[1,4] Shruti Menon,[2,4] Jana Dobrovolna,[3] Ralph Imhof,[1] Pavel Janscak,[2,3] Tuncay Baubec,[1] and Matthias Altmeyer[1,5,*]
[1]Department of Molecular Mechanisms of Disease, University of Zurich, 8057 Zurich, Switzerland
[2]Institute of Molecular Cancer Research, University of Zurich, 8057 Zurich, Switzerland
[3]Institute of Molecular Genetics, Academy of Sciences of the Czech Republic, Videnska 1083, 143 00 Czech Republic
[4]Life Science Zurich Graduate School (LSZGS), 8057 Zurich, Switzerland
[5]Lead Contact
*Correspondence: matthias.altmeyer@uzh.ch
https://doi.org/10.1016/j.molcel.2018.11.036

SUMMARY

Cellular mechanisms that safeguard genome integrity are often subverted in cancer. To identify cancer-related genome caretakers, we employed a convergent multi-screening strategy coupled to quantitative image-based cytometry and ranked candidate genes according to multivariate readouts reflecting viability, proliferative capacity, replisome integrity, and DNA damage signaling. This unveiled regulators of replication stress resilience, including components of the pre-mRNA cleavage and polyadenylation complex. We show that deregulation of pre-mRNA cleavage impairs replication fork speed and leads to excessive origin activity, rendering cells highly dependent on ATR function. While excessive formation of RNA:DNA hybrids under these conditions was tightly associated with replication-stress-induced DNA damage, inhibition of transcription rescued fork speed, origin activation, and alleviated replication catastrophe. Uncoupling of pre-mRNA cleavage from co-transcriptional processing and export also protected cells from replication-stress-associated DNA damage, suggesting that pre-mRNA cleavage provides a mechanism to efficiently release nascent transcripts and thereby prevent gene gating-associated genomic instability.

INTRODUCTION

Cell growth and proliferation involve ordered progression through different cell-cycle stages. During cell-cycle progression, the genome undergoes considerable changes, which affect its structure and function. Faithful DNA replication during S phase represents a serious challenge for genome integrity. Hundreds of replication forks, fired from many different origins, simultaneously move through the mammalian genome, copying the genetic information with high speed and exquisite fidelity (Saldivar et al., 2017; Técher et al., 2017). This process is not only tightly regulated and coordinated with other genome functions, but also dynamically buffered, allowing it to flexibly react to obstacles and difficult to replicate regions. The flexibility stems, in parts, from an excess number of origins (Alver et al., 2014), and from a surplus of replication protein A (RPA), which shields single-stranded DNA (ssDNA) occurring as physiological replication intermediate and at enhanced levels when replication forks stall (Toledo et al., 2013). The key function of the replication checkpoint is to ensure that replication fork stability and origin firing are coordinated in a way that does not exhaust the cellular capacity to globally protect replication forks (Saldivar et al., 2017; Toledo et al., 2013). While recent studies uncovered a plethora of pathways that act directly at replication forks to maintain fork stability and protect stalled forks from nucleolytic degradation (Berti and Vindigni, 2016; Cortez, 2015; Pasero and Vindigni, 2017), the thresholds determining replication capacity nucleus-wide and how they are being altered under pathological conditions are still poorly defined.

Cancer cells exploit the replication buffering system for their needs, allowing them to proliferate at higher rates and with altered replication timing. While accelerated proliferation and the ensuing replication stress (RS), often triggered by oncogene activation (Hills and Diffley, 2014; Macheret and Halazonetis, 2015), promote accumulation of mutations and thereby drive cancer development, staying within the physiological thresholds of replication capacity is crucial for cancer cell survival. Thus, understanding the intrinsic thresholds of replication capacity is a prerequisite to chart cancers according to their relative replication stress state. Indeed, current approaches in cancer therapy aim at exploiting elevated levels of replication stress present in different cancers by employing replication drugs and checkpoint inhibitors to push cancer cells into a state of irreversible genome damage (Dobbelstein and Sørensen, 2015; O'Connor, 2015). However, in most cases it is insufficiently understood how cancer-specific changes impact replication capacity and replication stress resilience.

Here, we employed a convergent multi-screening approach to assess replication capacity and replication stress sensitivity upon loss of a class of recently identified, recurrently mutated cancer genes. Multidimensional phenotypic readouts enabled us to chart detailed maps of cell-cycle phase distribution, replication speed, RPA exhaustion, and DNA damage signaling in

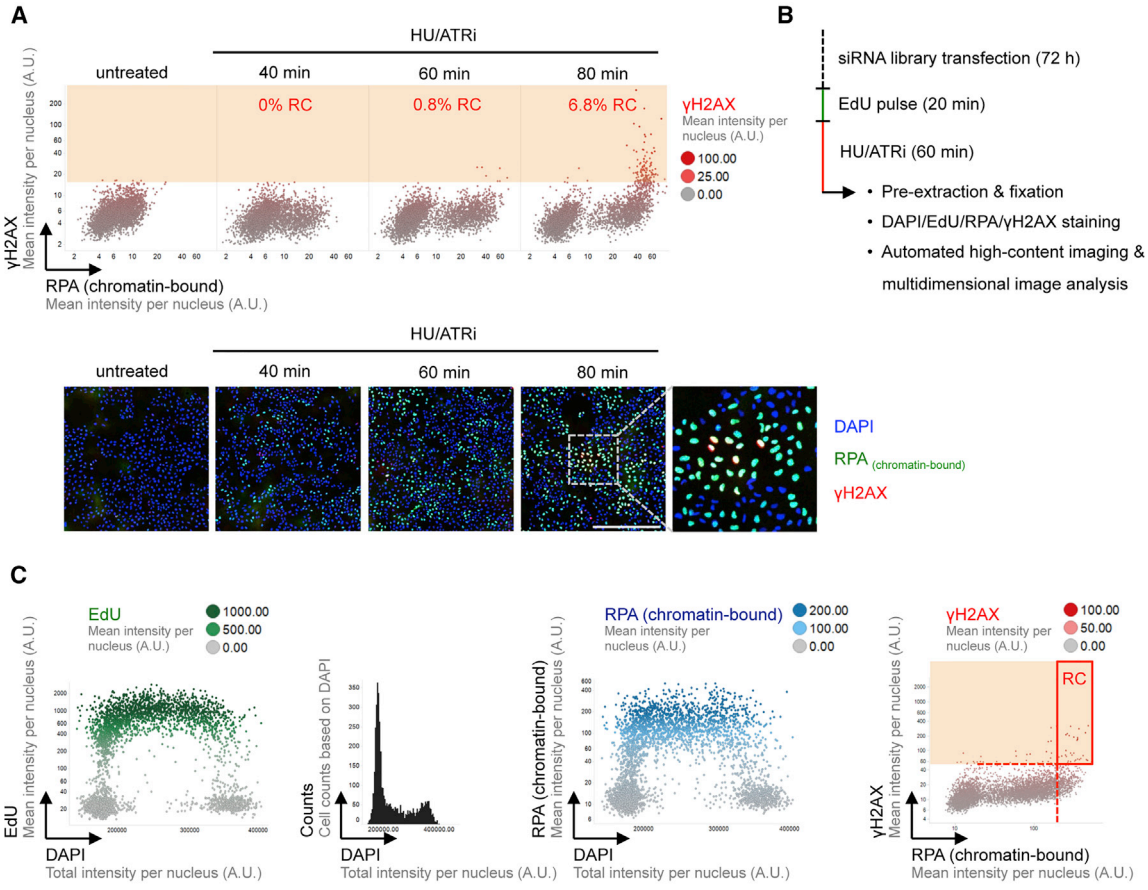

GO biological process	P-value
Gene expression (GO:0010467)	7.26E-15
Nucleic acid metabolic process (GO:0090304)	1.43E-14
Cellular nitrogen compound metabolic process (GO:0034641)	1.59E-13
RNA metabolic process (GO:0016070)	2.69E-13
Cellular macromolecule metabolic process (GO:0044260)	7.27E-13

(legend on next page)

large cell populations and on a gene-by-gene basis. Among the factors that we identified to confer resistance to replication stress was the polyadenylation signal recognizing subunit of the cleavage and polyadenylation complex, WDR33, which we show is required to prevent THO nuclear export complex (THOC)-mediated re-localization of nascent transcripts and genomic loci toward the nuclear periphery and thereby protects from replication stress-associated DNA damage.

RESULTS

A Convergent Multi-screening Approach Identifies Cancer Genes with Roles in Replication Stress Resilience

Dedicated cellular mechanisms exist to stabilize stalled replication forks and restore their function (Zeman and Cimprich, 2014). One common endpoint of acute, severe replication stress is the nucleus-wide exhaustion of RPA due to excessive amounts of ssDNA upon replication fork stalling, which is followed by massive chromosome breakage (Toledo et al., 2013). Scoring the degree of RPA sequestration in conjunction with markers of DNA damage signaling thus provides a means to assess sensitivity and resilience to replication stress-induced replication catastrophe (RC). Combining the antimetabolite hydroxyurea (HU) to deplete nucleotides and stall replication forks (Figure S1A) with short-term inhibition of the replication checkpoint kinase ATR (ATRi) (Toledo et al., 2013), we established conditions in which S phase cells were just at the tipping point between maximal RPA chromatin loading and RC (Figures 1A and S1B). We then designed a targeted small interfering RNA (siRNA) library covering a class of newly emerging, recurrently mutated cancer genes (Davoli et al., 2013; Lawrence et al., 2014; Nijhawan et al., 2012; Zack et al., 2013), using three individual siRNAs against each target gene (Table S1). 72 hr after siRNA transfection, we applied a 5-Ethynyl-2'-deoxyuridine (EdU) pulse to measure replication capacity followed by a short-term HU plus ATRi treatment (Figure 1B). Using high-content microscopy for quantitative image-based cytometry (QIBC) (Altmeyer et al., 2013; Toledo et al., 2013), we simultaneously assessed survival, cell-cycle distribution, replication competence, RPA loading, and DNA damage signaling (Figure 1C), altogether taking around 26 million measurements across almost 2 million single cells with an average of 4,500 cells per condition. Reassuringly, when ranked according to a *Z* score of cells in RC, the checkpoint kinase ATR, whose inhibition or partial depletion primes cells to undergo RC (Toledo et al., 2013) and which was used as positive control, scored highly with three out of three siRNAs (Figure 1D; Table S2). Gene ontology (GO) analysis of replication stress resilience modulators revealed that they were enriched for genes involved in DNA and RNA metabolism (Figure 1E), consistent with previous work (Kavanaugh et al., 2015; Paulsen et al., 2009). Interestingly, our data indicate that deregulated RNA metabolism can have both protective and sensitizing functions in the context of acute replication stress (Figures 1F and S1C), calling for detailed and gene-specific analyses of RNA processing factors and their roles in genome integrity maintenance. Moreover, we found no strong correlation between replication speed measured by EdU incorporation and replication stress sensitivity, suggesting that EdU incorporation alone is not a good marker for replication fidelity and replication stress resilience (Figure S1D).

Next, we designed multiple convergent screens using a sub-library of the original screen to consolidate and further extend the results. We first assessed the sensitivity to replication fork stalling by HU alone using RPA loading and γH2AX readouts (Figure S1E; Table S3). Then, we assessed the capacity to recover from acute replication stress by measuring EdU incorporation after transient HU-induced fork stalling (Figure S1F; Table S4). Finally, to assess the consequences of mild persistent replication stress, we turned to low doses of the polymerase inhibitor aphidicolin (APH) and quantified 53BP1 nuclear bodies in G1 cells as hallmarks of inherited damage from the previous S phase (Lukas et al., 2011), using cyclin A levels and DNA content for two-dimensional cell-cycle staging (Figure S1G; Table S5). The results of this multiple screening approach converged toward high-confidence modulators of replication stress resilience. One of the genes belonging to this category and scoring in all four screens is RTF1, a subunit of the PAF1 complex involved in transcriptional elongation, which was recently linked to replication stress resilience in yeast (Poli et al., 2016). A second gene that scored highly in all our screens was the cleavage and polyadenylation complex (CPC) component WDR33, a WD40 RNA-binding protein that directly recognizes the poly(A) signal and thus connects the cleavage and polyadenylation complex to nascent mRNAs at the 3′ end of protein-coding genes (Chan et al., 2014; Schönemann et al., 2014). WDR33 was identified as haploinsufficient tumor suppressor gene in a pan cancer genome sequencing analysis scoring comparable to other well-established tumor suppressors such as 53BP1, BRCA1, and BRCA2 (Davoli et al., 2013). However, potential roles of WDR33 in genome integrity maintenance have remained uncharacterized.

Figure 1. A Convergent Multi-screening Approach Identifies Cancer Genes with Roles in Replication Stress Resilience

(A) Asynchronously growing U-2 OS cells were treated as indicated and assessed for chromatin-bound RPA and γH2AX signaling by QIBC. Each dot represents a single cell, color-coded according to γH2AX levels as indicated. Percentages of cells in RC, marked by RPA exhaustion and γH2AX formation, are provided. Large fields of view of representative cell populations are provided below. Scale bar, 500 μm. See STAR Methods for further details.

(B) Experimental scheme for the siRNA screen.

(C) Overview of the multi-dimensional readouts employed to screen for modulators of replication stress (RS) resilience using the negative control condition as example. For each well, 5-Ethynyl-2'-deoxyuridine (EdU) incorporation, cell cycle, RPA retention on chromatin, and γH2AX signaling were quantified.

(D) *Z* score according to percentage of cells in RC.

(E) Gene ontology (GO) analysis of identified modulators of replication stress resilience.

(F) Range of phenotypes from promoter and suppressor genes. Representative images are shown on the right. Scale bar, 100 μm.

See also Figure S1 and Tables S1, S2, S3, S4, and S5.

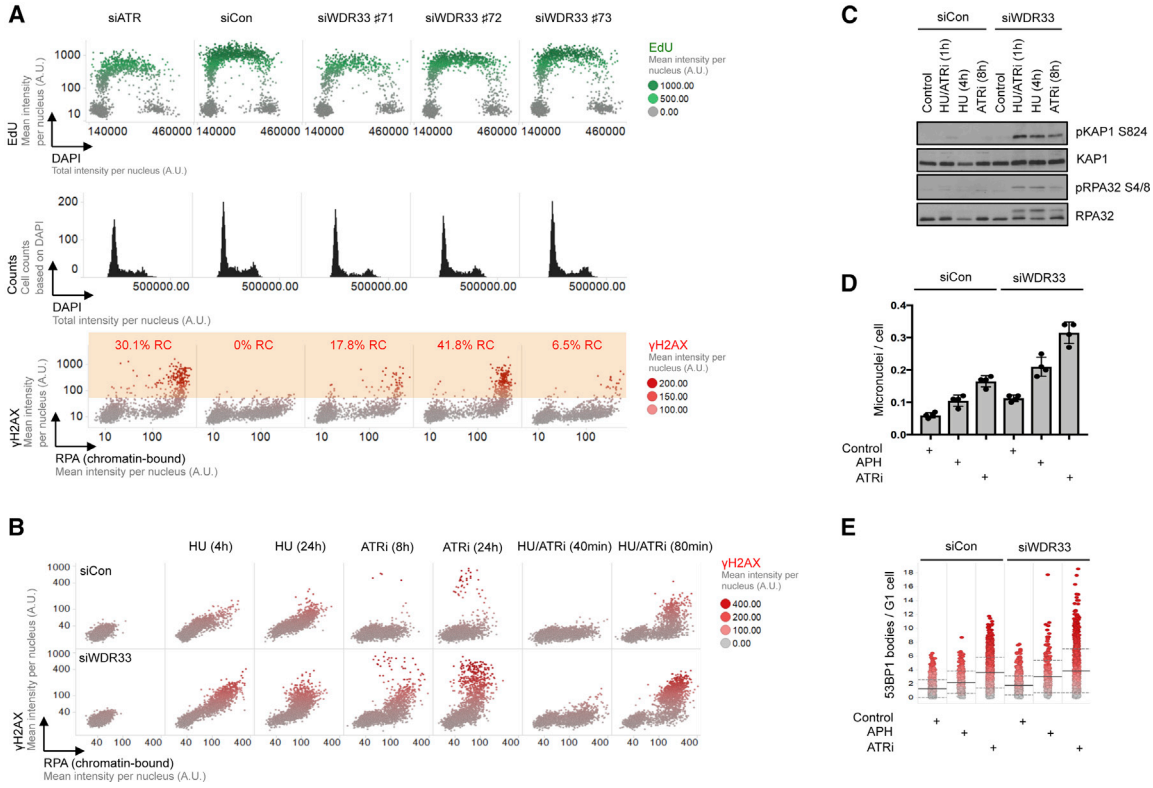

Figure 2. The Cleavage and Polyadenylation Factor WDR33 Protects Cells from Replication Stress

(A) Comparison of EdU, cell cycle, and RC profiles of control, ATR-depleted, and WDR33-depleted cells using three independent siRNAs. Cells were labeled with EdU for 20 min prior to HU plus ATRi exposure for 1 hr. Percentages of S phase cells in RC are provided.

(B) Replication stress sensitivity of WDR33-depleted cells upon single and combined HU and ATRi treatments.

(C) Western blot analysis of the DNA damage markers pKAP1 (S824) and pRPA (S4/8) in HU, ATRi, and HU plus ATRi-treated cells.

(D) Micronuclei formation upon 24-hr ATRi or aphidicolin (APH) treatment.

(E) Formation of 53BP1 nuclear bodies in G1 cells upon 24-hr ATRi or APH treatment. Solid and dotted lines indicate averages ±SD, respectively.

See also Figure S2 and Table S6.

The Pre-mRNA Cleavage Factor WDR33 Protects Cells from Replication Stress

Reanalysis of our screening data showed that cells upon WDR33 depletion replicate normally and have normal cell-cycle profiles, yet when challenged by replication stress are prone to experience RC at greatly accelerated rate (on average 22% of S phase cells in RC versus 0% in control conditions after 1 hr of treatment) (Figure 2A). The results were confirmed using a second ATRi (Figure S2A) and in different transformed and non-transformed cell lines (Figures S2B and S2C). The knockdown efficiency was controlled by western blot and by qPCR (Figures S2D and S2E). We re-tested the additional two WDR33-targeting siRNAs from our original screen and confirmed a pronounced sensitization to replication stress (Figures S2F–S2H). Similar results were obtained with a fourth siRNA and an endoribonuclease-prepared siRNA (esiRNA) pool against WDR33 (Figures S2I–S2J). Comparing cell lines stably expressing either siRNA-sensitive or -resistant GFP-WDR33 confirmed the specificity of this phenotype (Figures S2K and S2L). Extended time-course experiments revealed that WDR33 depletion sensitizes cells to HU plus ATRi combined treatment as well as to single HU or ATRi exposure, increasing both RC entry (Figure 2B) and ssDNA accumulation (Figure S2M). The sensitivity in short-term experiments translated to a survival defect in clonogenic assays (Figure S2N). Western blot analysis of the DNA damage markers phospho-KAP1 (pKAP1) and phospho-RPA (pRPA) confirmed the conclusion of our QIBC results, namely, that WDR33-depleted cells enter a state of enhanced replication stress-induced DNA damage (Figure 2C). Furthermore, when scoring micronuclei formation and 53BP1 nuclear bodies in G1 cells, we observed that both markers were elevated in WDR33-depleted cells upon replication stress challenges, implying a function of WDR33 in maintaining genome stability (Figures 2D and 2E).

The finding that deregulated WDR33 function sensitizes cells to ATRi seemed particularly interesting given that ATRi have recently entered clinical trials for cancer treatment (Karnitz and Zou, 2015). To interrogate drug sensitivities evoked by WDR33 depletion more broadly, we exposed cells to a panel of epigenetic drugs, replication and checkpoint inhibitors, and other genotoxic agents (Table S6). This confirmed the sensitivity to ATRi and HU and revealed additional sensitivities to the CHK1 inhibitor UCN-01 and the two nucleoside analogs gemcitabine and

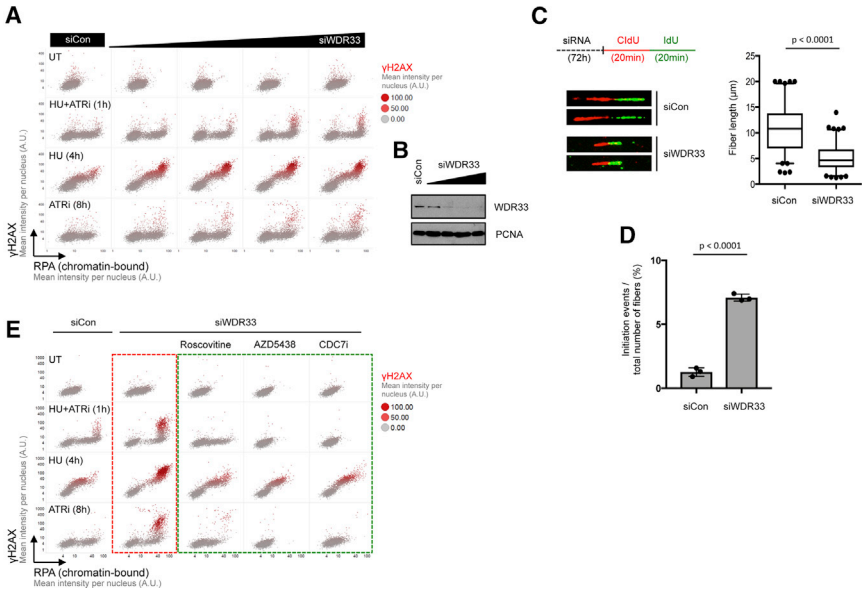

Figure 3. Impaired WDR33 Function Results in Reduced Replication Fork Speed and Excessive Origin Firing

(A) Titration of WDR33 siRNA (0.1, 0.5, 2.5, and 5 nM) results in a gradual sensitization of cells to replication stress treatments.

(B) Western blot of WDR33 levels upon gradual siRNA-mediated depletion.

(C) DNA fiber assay to monitor replication fork speed. Cells were treated with siRNA and 5-Chloro-2'-deoxyuridine-Iododeoxyuridine (CldU-IdU) as indicated, and fiber track lengths were measured.

(D) Origin firing was assessed by scoring replication initiation events as percentage of the total number of DNA fibers analyzed.

(E) CDK inhibition rescues WDR33-depleted cells from RC. Cells were treated with siRNA as indicated and the CDK inhibitors Roscovitine and AZD5438, or the CDC7 inhibitor PHA-767491, were added for 8 hr in conjunction with the indicated replication stress treatments.

See also Figure S3.

cytarabine, suggesting that reduced WDR33 levels specifically sensitize cells to clinically relevant replication drugs and checkpoint inhibitors (Figure S2O).

In line with the established role of WDR33 in pre-mRNA cleavage (Chan et al., 2014; Schönemann et al., 2014), endogenous WDR33 co-immunoprecipitated the polyadenylation specificity factors CPSF30, CPSF160, and FIP1 (Figure S2P). Reassuringly, depletion of CPSF30, CPSF160, or FIP1, which were not covered by our original screen, gave similar replication stress phenotypes as WDR33 knockdown (Figures S2Q–S2S).

Impaired WDR33 Function Results in Reduced Replication Fork Speed and Excessive Origin Firing

Given that WDR33 is essential for cell survival (Hart et al., 2015; Wang et al., 2015) and in light of its potential role as haploinsufficient tumor suppressor (Davoli et al., 2013), we aimed to mimic haploinsufficiency by partial WDR33 depletion. This revealed that incomplete loss of WDR33 is sufficient to confer replication stress sensitivity and that the degree of sensitivity increases with the degree of WDR33 depletion (Figures 3A and 3B). To mechanistically dissect the role of WDR33 in replication stress resilience, we first analyzed S phase checkpoint activation. We observed no sign of checkpoint signaling (assessed by CHK1 phosphorylation status) in unchallenged WDR33-depleted cells, and CHK1 phosphorylation upon induced replication stress was comparable to control cells (Figure S3A). DNA fiber experiments to monitor replication fork progression revealed, however, that WDR33-depleted cells exhibited greatly reduced fork speed (Figure 3C), which was accompanied by excessive origin firing (Figure 3D). Replication fork progression and stability is modulated by fork reversal and fork degradation and deregulated fork reversal or unrestrained fork degradation can cause DNA damage and genome instability (Berti and Vindigni, 2016). While we observed excessive fork degradation in BRCA2-depleted cells as well as unrestrained fork progression upon Poly(ADP-ribose) polymerase (PARP) inhibition as described before (Berti et al., 2013; Schlacher et al., 2011), WDR33 depletion had no significant effect in these assays, suggesting that fork slowing in WDR33-deficient cells occurs via a different mechanism (Figures S3B and S3C). We next measured RPA foci numbers at early time points after HU-induced fork stalling, before cells start to enter RC, as a proxy for fork uncoupling in replication factories. While WDR33-depleted cells were indistinguishable from control cells in unchallenged conditions, already 1 hr after HU a pronounced increase in RPA foci could be observed, which escalated over time (Figure S3D). We next tested whether chemical inhibition of origin firing could alleviate replication stress sensitivity. While inhibition of cyclin-dependent kinases (CDKs) did not affect fork speed in WDR33-depleted cells (Figure S3E), two unrelated CDK inhibitors rescued WDR33-defective cells from RC (Figure 3E). Consistently, both chemical inhibition of the replication initiation kinase CDC7 and titrated depletion of the initiation factor CDC45 gave similar results (Figures 3E and S3F). Conversely, gradual depletion of RPA, which buffers against origin firing-related replication stress (Toledo et al., 2013), synergized with WDR33 depletion to force cells into RC (Figure S3G). Taken together, these data indicate that excessive origin firing drives replication stress sensitivity of WDR33-depleted cells.

RNA:DNA Hybrids Form in WDR33-Depleted Cells as a Consequence of RC

Transcription-associated R-loops are a source of genomic instability and can lead to transcription-replication conflicts and DNA breakage (Gaillard and Aguilera, 2016; Sollier and Cimprich, 2015). Given the role of WDR33 in co-transcriptional pre-mRNA processing, we aimed to investigate a potential role of R-loops in the observed genomic instability phenotype of WDR33-depleted cells. RNaseH1 binds and resolves R-loops, and inactive RNaseH1 mutants can be used to detect RNA:DNA

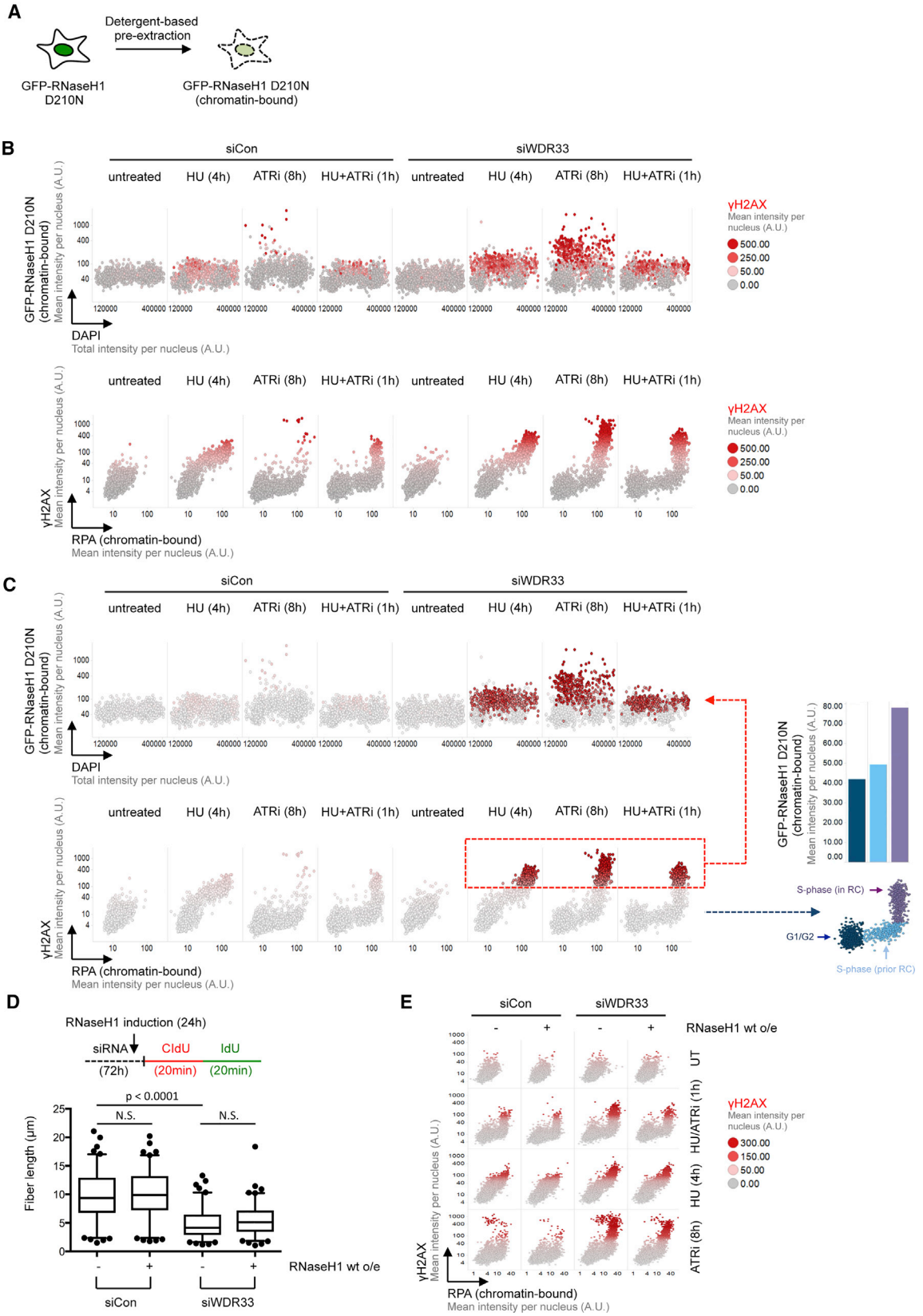

(legend on next page)

hybrids (Chen et al., 2017; Tresini et al., 2015). We employed a stable cell line for doxycycline-inducible expression of the inactive RNaseH1 D210N mutant (Figure S4A) and exploited its enhanced chromatin retention upon RNA:DNA-hybrid recognition to monitor hybrid formation by automated high-content microscopy (Figures 4A and S4B). This revealed the formation of RNA:DNA hybrids, specifically in S phase cells, and their dynamics upon different replication stress treatments (Figure S4C). Strikingly, WDR33-depleted cells showed a marked increase in hybrid formation (Figure 4B). More detailed cell-cycle-resolved analyses of hybrid formation, RPA exhaustion, and DNA damage signaling in time-course experiments revealed that the most prominent increase in hybrid formation was always confined to the sub-population of cells that had exhausted their RPA pool and underwent RC (Figures 4C and S4D–S4F). Similar results were obtained when using the S9.6 antibody to detect RNA:DNA hybrids (Figures S4G and S4H). Consistently, doxycycline-induced overexpression of wild-type RNaseH1 (Figure S4I), despite being able to rescue R-loop-associated KAP1 phosphorylation upon knockdown of Aquarius (Sollier et al., 2014; Figure S4J), had no significant effect on replication fork speed in WDR33-depleted cells (Figure 4D) and only mildly rescued from RC (Figure 4E). Inhibition of origin firing, however, completely abolished RNA:DNA-hybrid formation in WDR33-depleted cells (Figures S4K and S4L). While these results do not exclude roles of RNA:DNA hybrids in triggering genomic instability, they indicate that a significant fraction of replication stress-associated hybrids in WDR33-depleted cells coincides with RC.

Transcription Inhibition Rescues Fork Speed, Excessive Origin Activation, and Replication Stress Sensitivity upon Deregulated Pre-mRNA Cleavage

Defective pre-mRNA cleavage can be expected to impair transcription termination, with nascent transcripts remaining bound to the elongating RNA polymerase II (RNA Pol II). Consistently, WDR33-depleted cells showed impaired polyadenylation and delayed mRNA export (Figures S5A and S5B). This prompted us to perform chromatin immunoprecipitation sequencing (ChIP-seq) experiments for the elongating form of RNA Pol II (RNA Pol II pS2), in order to identify genomic regions of impaired transcription termination. WDR33 loss led to clear changes in RNA Pol II dynamics, with the elongating polymerase often spreading far beyond termination zones (Figures 5A, 5B, S5C, and S5D). The affected genes clustered into five groups, three of which were characterized by a pronounced broadening of the termination zone (Figures 5C and S5E; Table S7). They did not differ significantly in activity or distance to neighboring genes and showed only mild differences in gene length (Figures 5D and S5F). The global changes in RNA Pol II occupancy were recapitulated by increased levels of RNA Pol II on the chromatin of WDR33-depleted cells, a phenotype that was reversed by transcription inhibition using 5,6-Dichlorobenzimidazole 1-β-D-ribofuranoside (DRB) (Figures S5G–S5I). DRB treatment also rescued the reduced replication fork speed in WDR33-depleted cells, suppressed excessive origin firing, and alleviated replication stress sensitivity and entry into RC (Figures 5E, 5F, and S5J). Similar results were obtained with the transcription inhibitor flavopiridol (Figures 5G, S5K, and S5L). Thus, faithful recognition of the poly(A) signal by WDR33 is pivotal for efficient termination and RNA Pol II turnover, which in turn is required to assure speedy replication fork progression and temperate origin usage.

Impaired Pre-mRNA Cleavage Unveils a Gene Gating-Resembling Mechanism in Mammalian Cells

When devising different scenarios of how defective pre-mRNA cleavage could lead to transcription-replication interference, we considered the possibility that unreleased chromatin-bound transcripts could pose a problem for the approaching replication machinery. More specifically, we considered that unreleased transcripts, due to the coupled action of the mRNA maturation and export machinery, might re-localize associated genomic loci toward the nuclear periphery and thereby challenge replication fork progression. Such a situation is not completely unprecedented, as previous work in yeast established that gene gating at nuclear pore complexes needs checkpoint functions to be relieved for replication forks to pass by (Bermejo et al., 2011). Consistently, loss of proteins, which tether nascent transcripts to the nuclear periphery, such as THO, TREX-2, or inner-basket nucleoporins, was found to be synthetically viable with loss of the checkpoint kinase Rad53 (Bermejo et al., 2011). We observed that checkpoint-inhibited WDR33-depleted cells accumulated a significant amount of RPA foci directly at the nuclear periphery, even when cells were deliberately matched for similar overall RPA foci counts prior to RC (Figures 6A and 6B). Furthermore, a stably integrated LacO array (Tang et al., 2013), which in the absence of DNA damage was transcriptionally repressed but not completely silent, localized closer to the nuclear periphery in WDR33-depleted cells as compared to control cells, despite these cells being indistinguishable in nuclear area (Figures 6C, S6A, and S6B). Similar results were obtained when we assessed nascent transcripts marked by the RNA-binding MS2 protein (Janicki et al., 2004; Shanbhag et al., 2010) and measured their distance to the nuclear periphery (Figures 6D

Figure 4. RNA:DNA Hybrids in WDR33-Depleted Cells Are Associated with RC

(A) Scheme for the inducible GFP-RNaseH1 D210N cell line to detect RNA:DNA hybrids. After exposure to doxycycline for 24 hr, cells are pre-extracted and catalytically inactive, chromatin-bound GFP-RNaseH1 D210N can be quantified by QIBC.

(B) The formation of RNA:DNA hybrids was assessed in a cell-cycle-resolved manner by high-content microscopy-based quantification of chromatin-retained GFP-RNaseH1 D210N (top panels). In the same cells, RC was also analyzed (bottom panels).

(C) For the same samples in (B), cell populations were divided into G1/G2 (no detectable RPA chromatin loading), S phase prior to RC (RPA loading, no γH2AX induction), and S phase after RC (maximal RPA loading, high levels of DNA damage signaling), and the respective levels of RNA:DNA hybrids were quantified.

(D) Wild-type GFP-RNaseH1 was overexpressed for 24 hr as indicated, and replication fork speed was measured by fiber assays.

(E) Wild-type GFP-RNaseH1 was overexpressed for 24 hr as indicated, and RC was analyzed upon different replication stress treatments.

See also Figure S4.

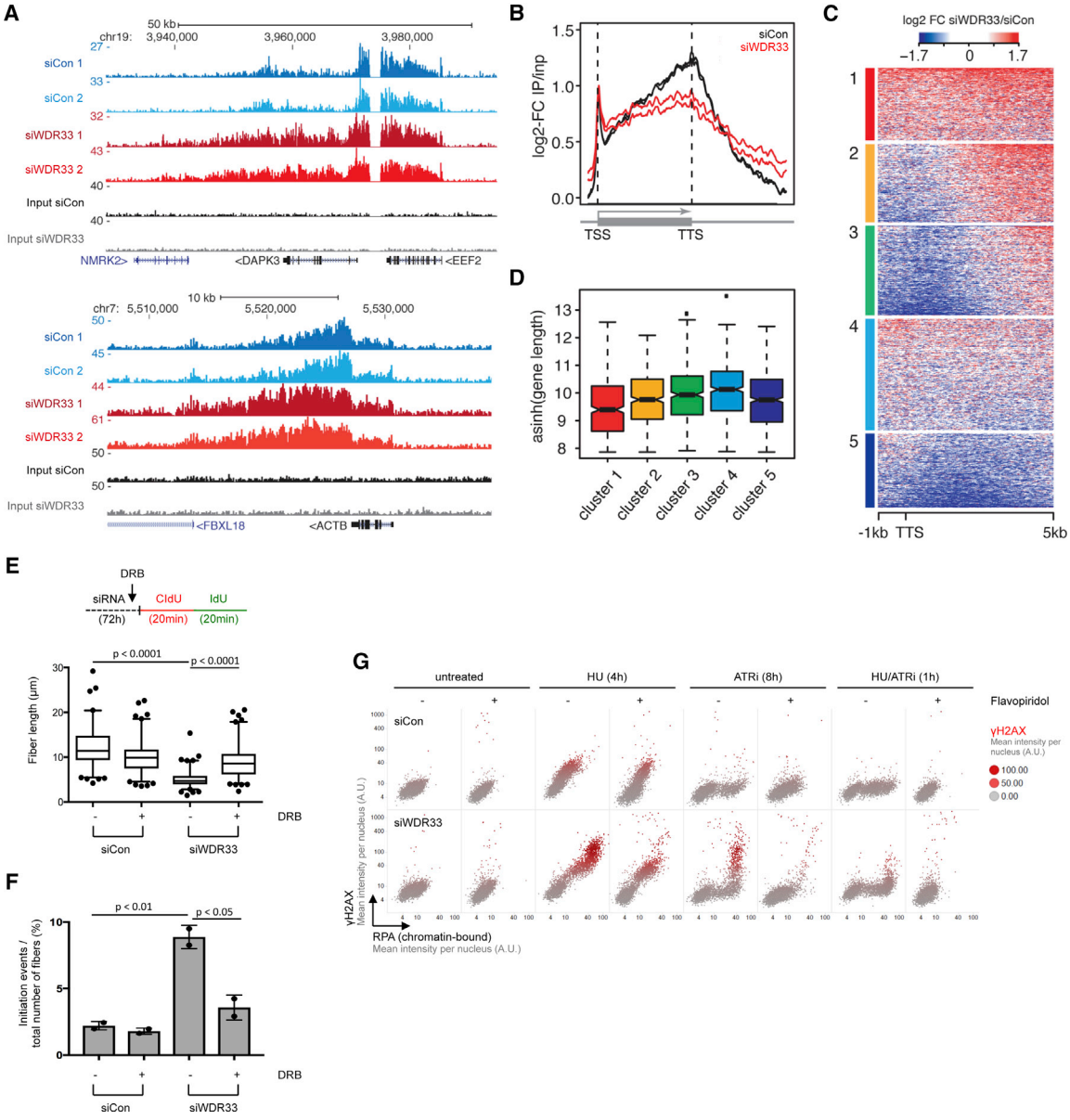

Figure 5. Transcription Inhibition Rescues Fork Speed, Excessive Origin Activation, and Replication Stress Sensitivity upon Deregulated Cleavage and Polyadenylation

(A) Representative genome browser views of RNA Pol II pS2 distribution. Depicted are sequencing read coverage per 100-bp bins obtained from two independent ChIP experiments (r1 and r2). Input tracks indicate coverages obtained from non-enriched chromatin samples.

(B) Average density profile summarizing global changes in RNA Pol II pS2 distribution along active genes. Shown are average log2 enrichments over corresponding input and normalized to gene length.

(C) Unsupervised clustering based on RNA Pol II pS2 log2-fold changes separates active genes into five distinct clusters. Clustering was calculated based on ChIP-seq signals −1 kb upstream and 5 kb downstream of the TTS. Clusters 1–3 are characterized by enhanced RNA Pol II spreading downstream of the TTS in WDR33-depleted cells.

(D) Boxplots showing the distribution of transcript length for the five clusters. Boxes show the interquartile range (IQR), whiskers denote the IQR × 1.5 range, and outliers are indicated by individual data points. Transcript size values (in bp) have been transformed for better visualization.

(E) Replication fork speed is rescued by transcription inhibition. Cells were treated as indicated in the absence or presence of DRB for the last 8 hr, and replication fork speed was measured by DNA fiber analysis.

(F) Origin firing was assessed by scoring replication initiation events as percentage of the total number of DNA fibers analyzed.

(G) Transcription inhibition rescues WDR33-depleted cells from RC. Cells were treated with siRNA, HU, ATRi, or HU plus ATRi and Flavopiridol (8 hr) as indicated, and entry into RC was scored.

See also Figure S5 and Table S7.

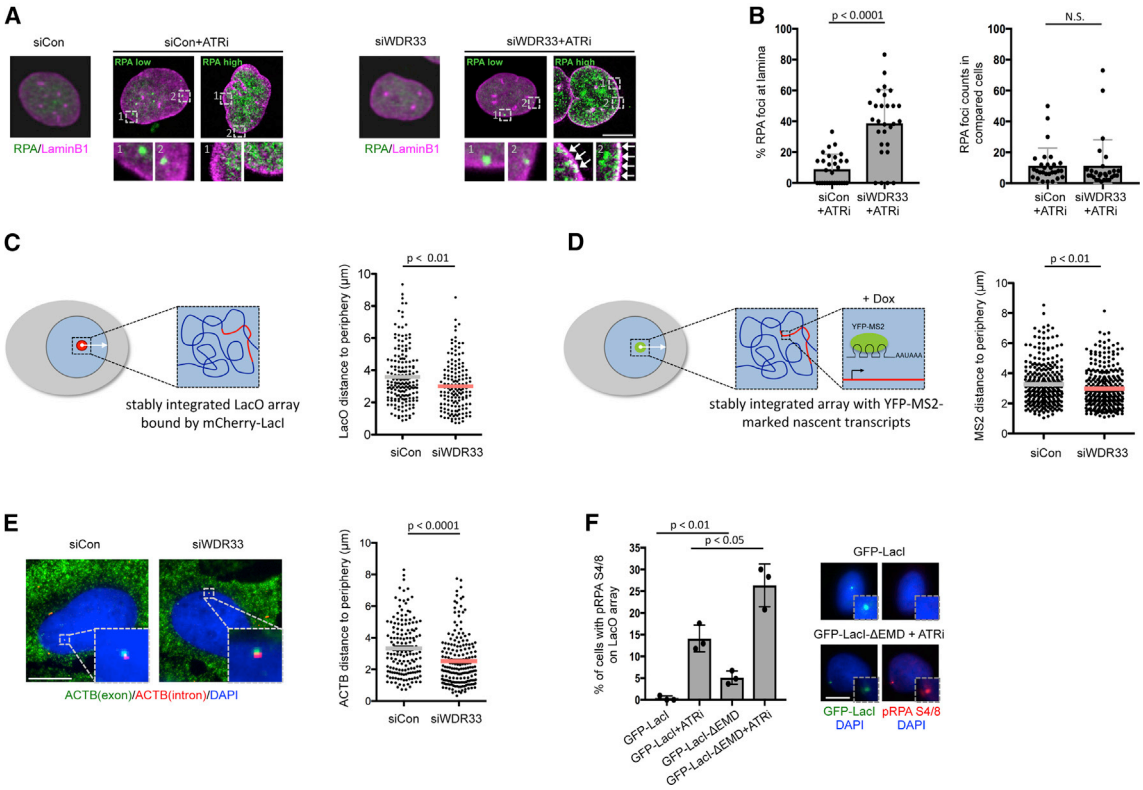

Figure 6. WDR33 Deficiency Is Linked to Gene Re-localization and Chromosome Fragility at the Nuclear Periphery

(A) Cells were treated as indicated, and RPA foci formation was assessed by confocal microscopy in LaminB1 co-stainings. To correct for the enhanced replication stress sensitivity upon WDR33 depletion, cells with similar RPA patterns were compared.

(B) Quantification of ATRi-induced RPA foci co-localizing with LaminB1 in cells deliberately matched for their overall RPA foci counts prior to RC, corresponding to RPA low samples in (A).

(C) Quantification of the closest distance of the center of the LacO array to the nuclear periphery in siCon and siWDR33 cells.

(D) Quantification of the closest distance of the center of the YFP-MS2 signal to the nuclear periphery 4 hr post induction in siCon and siWDR33 cells.

(E) RNA-FISH to identify transcriptionally active ACTB loci based on co-localization of FISH probes recognizing either mature ACTB mRNA (exon) or ACTB pre-mRNA (intron) transcript sequences. The closest distance of double-positive FISH signals to the nuclear periphery in siCon and siWDR33 cells was measured.

(F) The indicated cell lines were subjected to isopropyl-β-d-thiogalactopyranoside (IPTG) removal for 16 hr to allow LacI-LacO binding, and the percentage of cells with pRPA S4/8 at the LacI-marked locus was quantified. Scale bars, 10 μm.

See also Figure S6.

and S6C). Also, nascent ACTB transcripts, expressed from their endogenous genomic loci and visualized by RNA-fluorescence in situ hybridization (FISH), were closer to the nuclear periphery in WDR33-depleted cells (Figure 6E). Thus, both nascent transcripts and genomic loci are associated with the nuclear periphery when WDR33 function is impaired. Next, in a proof-of-concept experiment, we forced an interaction between the LacO array and the nuclear lamina using a previously employed Emerin C-terminal deletion (ΔEMD) fused to the GFP-LacI repressor (Lemaître et al., 2014; Reddy et al., 2008). The GFP-LacI-ΔEMD fusion was sufficient to re-localize the LacO array to the nuclear periphery (Figure S6D), consistent with earlier work (Lemaître et al., 2014; Reddy et al., 2008), and the peripheral tethering resulted in LacO-associated DNA damage marked by RPA S4/8 phosphorylation, particularly when ATR was inhibited (Figure 6F).

We therefore went on to test whether, similar to gene gating-associated replication stress in yeast (Bermejo et al., 2011), the THOC was involved in mediating the observed replication stress phenotypes in WDR33-deficient cells. Although THOC1 depletion on its own did not affect the localization of the LacO array (Figure S7A), loss of THOC1 in the absence of WDR33 rescued the re-localization of the LacO locus toward the nuclear periphery (Figure 7A). It also rescued the re-localization of MS2-marked transcripts (Figure 7B) and of endogenously expressed nascent ACTB transcripts (Figure 7C). Furthermore, THOC1 co-depletion rescued the peripheral RPA foci, which we had observed upon replication stress in WDR33-deficient cells (Figure 7D). Finally, THOC1 (or THOC2) co-depletion rescued replication fork speed (Figure 7E), excessive origin firing (Figure 7F), and alleviated replication stress sensitivity and entry into RC (Figure 7G). We confirmed the knockdown efficiency of the four siRNAs used against THOC1/2 and controlled that the efficiency of WDR33 depletion was unaffected (Figures S7B–S7D). We did not observe a rescue of the elevated levels of RNA Pol II on chromatin by THOC1 co-depletion (Figure S7E), yet consistent with

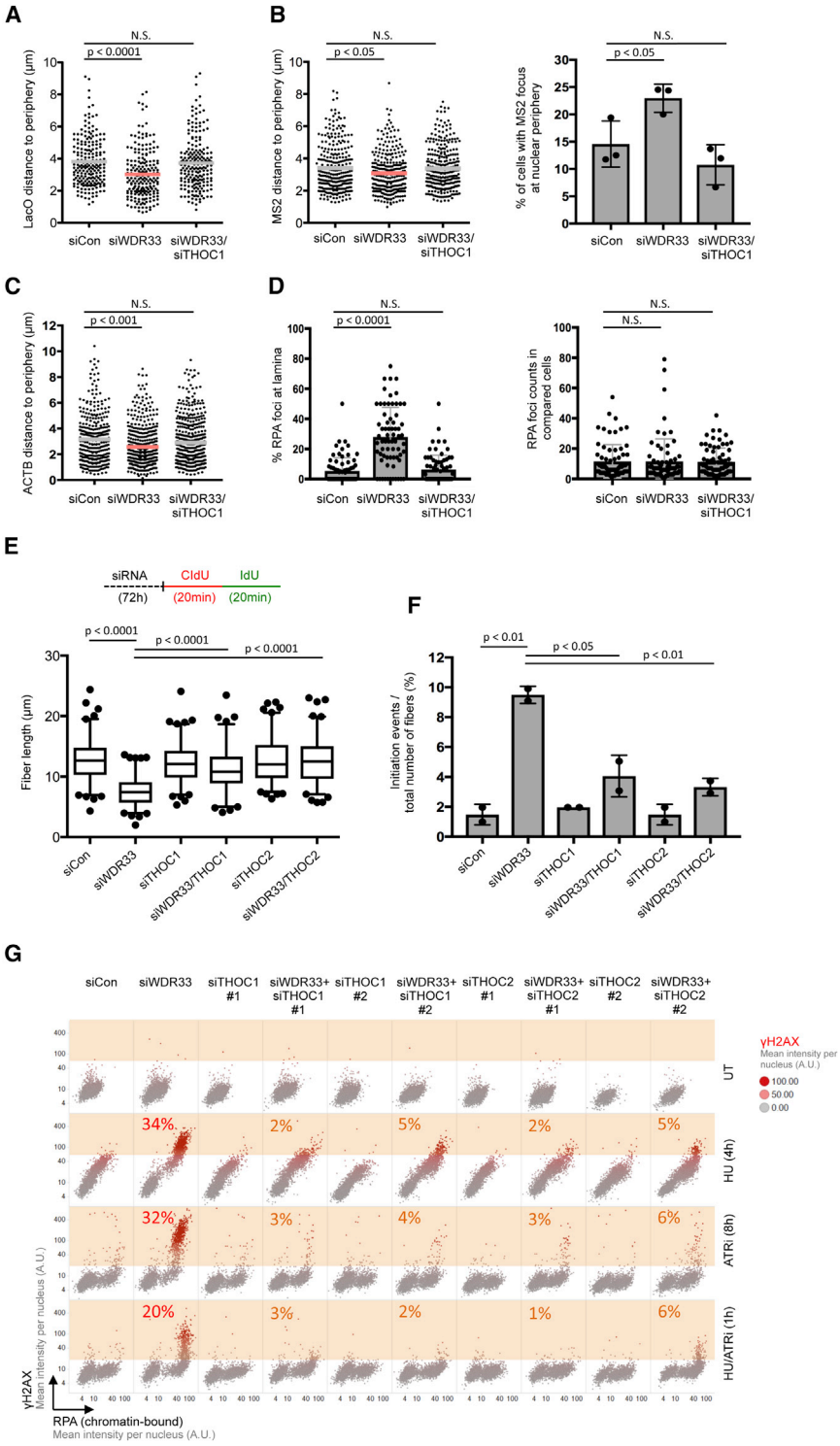

Figure 7. The THO Complex Drives Replication Stress Sensitivity When Pre-mRNA Cleavage Is Impaired

(A) Quantification of the closest distance of the center of the LacO array to the nuclear periphery upon co-depletion of WDR33 and THOC1.

(B) Quantification of the closest distance of the center of the YFP-MS2 signal to the nuclear periphery upon co-depletion of WDR33 and THOC1 (left panel), and quantification of the percentage of cells with the YFP-MS2 signal at the nuclear periphery upon WDR33 knockdown or co-depletion of WDR33 and THOC1 (right panel).

(C) Quantification of nascent RNA-FISH signals and their closest distance to the nuclear periphery upon WDR33 knockdown or co-depletion of WDR33 and THOC1.

(D) Quantification of peripheral RPA foci formation co-localizing with LaminB1 upon 8 hr ATRi after WDR33 knockdown or co-depletion of WDR33 and THOC1. Cells deliberately matched for their overall RPA foci counts prior to RC were analyzed.

(E) DNA fiber assay to monitor replication fork speed in WDR33-deficient cells with and without THOC1/2 co-depletion. Cells were treated with siRNA and CldU-IdU as indicated and fiber track lengths were measured.

(F) Origin firing was assessed by scoring replication initiation events as percentage of the total number of DNA fibers analyzed.

(G) Co-depletion of THOC1/2 rescues replication stress sensitivity in WDR33-deficient cells. U-2 OS cells were transfected as indicated and exposed to replication stress treatments, and RC was analyzed by QIBC. Percentages of cells in RC are provided.

See also Figure S7.

the QIBC results (Figure 7G) co-depletion of THOC1 rescued the levels of RPA S4/8 phosphorylation measured by western blot (Figure S7F) and relieved the ATRi-mediated survival defect in colony formation assays (Figure S7G). A similar rescue of replication stress sensitivity in WDR33-deficient cells was obtained when we co-depleted the TREX-2 component ENY2 or the nuclear pore complex proteins NUP153 and TPR (Figure S7H). Taken together, these data reveal a surprising functional ("synthetic viable") interaction between WDR33 and several components of the pre-mRNA processing and export machinery and suggest that efficient pre-mRNA cleavage and the release of nascent transcripts from chromosomes are essential to minimize the risk of replication stress-associated genome instability.

DISCUSSION

We used multidimensional high-content imaging in conjunction with a series of targeted siRNA screens to identify emerging cancer genes with roles in replication stress sensitivity and resilience. The siRNA approach allowed us to include a group of essential genes that is often deregulated in cancer yet easily escapes interrogation by gene knockout strategies including CRISPR-Cas9 screens.

Employing a stringent strategy of multiple convergent screens, we iteratively narrowed down the target hit list. While this does not derogate the importance of other candidates that scored in individual screens and/or with less than 3/3 siRNAs, it does provide an increased level of confidence in the identified genes as specific regulators of replication stress resilience. Indeed, one of the identified genes was the PAF1 complex subunit RTF1, and recent work in budding yeast demonstrated that the PAF1 complex functions together with Mec1 and the chromatin remodeler INO80 to protect cells from replication stress-induced DNA damage (Poli et al., 2016). In addition to RTF1, we identified WDR33, an integral component of the polyadenylation specificity factor that directly binds to the poly(A) motif (Chan et al., 2014; Schönemann et al., 2014). Structural studies recently illuminated how WDR33 cooperates with CPSF30 to bind to the 5′−AAUAAA-3′ hexanucleotide sequence (Clerici et al., 2017). However, not much is known about the consequences of deregulated WDR33 function in mammalian cells. Our work illustrates how impaired cleavage of nascent pre-mRNA slows down replication forks during S phase and leads to an increase in origin firing. This in turn renders cells highly sensitive to replication fork stalling drugs and replication checkpoint inhibitors.

An unexpected finding from our work was that cells with impaired pre-mRNA cleavage accumulate RNA:DNA hybrids when entering RC. R-loops have important yet insufficiently understood physiological functions, but they have also been shown to cause replication stress and represent an important source of genome instability (García-Muse and Aguilera, 2016; Sollier and Cimprich, 2015). While they are considered mostly as a driver of replication-transcription conflicts, our data suggest that significant amounts of RNA:DNA hybrids can also form as a consequence of DNA breakage upon replication stress-induced RPA exhaustion. Under conditions of RC, a large number of forks may break simultaneously (Toledo et al., 2013), generating free DNA ends that then become available for RNA to hybridize and generate break-induced RNA:DNA hybrids. Along the same lines, formation of RNA:DNA hybrids was recently discussed as potentially inevitable risk when DNA breaks occur in actively transcribed regions (Aguilera and Gómez-González, 2017), and it was reported that RNA Pol II is recruited to DNA double-strand breaks (DSBs) to initiate transcription and generate RNA:DNA hybrids (Cohen et al., 2018; D'Alessandro et al., 2018; Lu et al., 2018; Michelini et al., 2017). While our findings by no means exclude that hybrid formation can cause transcription-replication conflicts and lead to DNA breakage, e.g., upon head-on collisions between the replication and transcription machinery (Hamperl et al., 2017), they call for careful experimental assessment of whether or not RNA:DNA-hybrid formation is a cause or consequence of replication stress. We envision that in certain contexts hybrid formation can even be both cause and consequence, leading cells into a vicious cycle of R-loop-induced replication conflicts and DNA breakage followed by break-induced hybrid formation and potentially impaired DNA repair. Consistent with such a scenario, RNA:DNA hybrids formed prior to RC may directly contribute to RPA exhaustion by sequestering RPA on the displaced ssDNA (Nguyen et al., 2017).

The finding that excessive hybrid formation is associated with RC prompted us to consider the possibility that, upon defects in pre-mRNA cleavage, a mechanism resembling gene gating may lead to transcription-replication interference. Our data indeed support that impaired pre-mRNA cleavage results in re-localization of nascent transcripts and associated genomic loci toward the nuclear periphery, where they cause replication stress and DNA damage. We therefore suggest that efficient co-transcriptional pre-mRNA cleavage limits the risk for potentially harmful gene gating and is needed to ensure a maximum degree of freedom for chromatin movement, while at the same time promoting rapid pre-mRNA processing and export from the nucleus. While our data show that loss of THOC1/2 can rescue WDR33 deficiency and relieve replication stress sensitivity, in pre-mRNA cleavage-proficient cells the THO complex suppresses R-loops and promotes genome stability (Domínguez-Sánchez et al., 2011; García-Benítez et al., 2017; Salas-Armenteros et al., 2017). Thus, depending on the status and working capacity of the pre-mRNA cleavage machinery, THOC may have either protective or adverse functions for genome integrity.

The essential kinase ATR plays multiple roles in protecting replication forks, regulating origin firing and activation of cell-cycle checkpoints (Buisson et al., 2015, 2017; Dungrawala et al., 2015; Saldivar et al., 2017, 2018; Yazinski and Zou, 2016), and its inhibition has become a promising avenue for the treatment of cancers with elevated levels of replication stress (Karnitz and Zou, 2015; Lecona and Fernandez-Capetillo, 2018). Besides the checkpoint function needed to resolve gene gating-associated replication stress in yeast (Bermejo et al., 2011), ATR also senses and is activated by mechanical stress directly at the nuclear envelope (Kumar et al., 2014). Further, we note that unbiased phospho-proteomics studies showed that DNA damage response (DDR) kinases modify several components of the pre-mRNA processing and export machinery, as well as key constituents of the nuclear pore complex (Beli et al., 2012; Blasius et al., 2011; Matsuoka et al., 2007). We therefore envision that analogous to the situation in yeast (Bermejo et al., 2011) ATR-dependent phosphorylation of proteins involved in pre-mRNA processing and export may be needed to relieve the stress associated with unreleased nascent transcripts under conditions when pre-mRNA cleavage is impaired or its capacity becomes limiting.

STAR★METHODS

Detailed methods are provided in the online version of this paper and include the following:

- KEY RESOURCES TABLE
- CONTACT FOR REAGENTS AND RESOURCE SHARING
- EXPERIMENTAL MODEL AND SUBJECT DETAILS
  - Cell lines
  - Bacterial strains
- METHOD DETAILS
  - pAcGFP-WDR33 cloning
  - Generation of GFP-WDR33 cell lines
  - Generation of GFP-RNaseH1 cell lines
  - EdU/EU labeling and BrdU incorporation
  - Drug treatments

- siRNA transfections
- Immunostaining
- DNA-FISH
- RNA-FISH
- DNA fiber analysis
- Quantitative image-based cytometry (QIBC)
- Confocal microscopy
- Chromatin fractionation
- Immunochemical methods
- Chromatin immunoprecipitation (ChIP)
- ChIP-sequencing and read processing
- Genomic coordinates and analysis at active genes
- RNA extraction and quantitative PCR (qPCR)
- Clonogenic survival assays
- Co-immunoprecipitation
- Mass spectrometry

- QUANTIFICATION AND STATISTICAL ANALYSIS
- DATA AND SOFTWARE AVAILABILITY

SUPPLEMENTAL INFORMATION

Supplemental Information includes seven figures and seven tables and can be found with this article online at https://doi.org/10.1016/j.molcel.2018.11.036.

ACKNOWLEDGMENTS

We are grateful to ScopeM, ZMB, and the FGCZ for excellent support. We thank R. Crouch for the RNaseH1 construct, E. Wahle for WDR33 cDNA, E. Soutoglou for GFP-LacI and GFP-LacI-ΔEMD cells, R. Greenberg for U-2 OS 2-6-3 cells, and M. Lopes and M. Berti for sharing protocols and reagents. We thank all members of our labs and of the DMMD for discussions and advice. Research in the lab of M.A. is supported by the Swiss National Science Foundation (SNSF, 150690 and 179057), the European Research Council (ERC) under the European Union's Horizon 2020 research and innovation program (ERC-2016-STG 714326), the Novartis Foundation for Medical-Biological Research (Grant 16B078), and the Swiss Foundation to Combat Cancer (Stiftung zur Krebsbekämpfung). J.M. is supported by the Gobierno Vasco Programa Posdoctoral de Perfeccionamiento de Personal Investigador Doctor. F.T. received support from the UZH Candoc Program (FK-16-053). Research in the lab of P.J. is supported by grants from the SNSF (31003A_166451), Swiss Cancer League (KFS-3802-02-2016), and the Czech Science Foundation (17-02080S), as well as the Neuron Fund for Support of Science and European Regional Development Fund/OP RDE (CZ.02.1.01/0.0/0.0/16_013/0001775) to J.D. Research in the lab of T.B. is supported by the SNSF (157488 and 180345).

AUTHOR CONTRIBUTIONS

J.D., S.M., and P.J. generated and validated the RNaseH1 cell lines. C.A. and T.B. performed ChIP experiments and analyzed genomics data. F.T., J.M., A.L., S.K., and R.I. designed and performed all other experiments and analyzed results. M.A., together with F.T., conceptualized the project. M.A. wrote the manuscript with edits from all authors and supervised the project.

DECLARATION OF INTERESTS

The authors declare no competing interests.

Received: April 16, 2018
Revised: August 31, 2018
Accepted: November 28, 2018
Published: January 10, 2019

REFERENCES

Aguilera, A., and Gómez-González, B. (2017). DNA-RNA hybrids: The risks of DNA breakage during transcription. Nat. Struct. Mol. Biol. *24*, 439–443.

Altmeyer, M., Toledo, L., Gudjonsson, T., Grøfte, M., Rask, M.B., Lukas, C., Akimov, V., Blagoev, B., Bartek, J., and Lukas, J. (2013). The chromatin scaffold protein SAFB1 renders chromatin permissive for DNA damage signaling. Mol. Cell *52*, 206–220.

Alver, R.C., Chadha, G.S., and Blow, J.J. (2014). The contribution of dormant origins to genome stability: From cell biology to human genetics. DNA Repair (Amst.) *19*, 182–189.

Beli, P., Lukashchuk, N., Wagner, S.A., Weinert, B.T., Olsen, J.V., Baskcomb, L., Mann, M., Jackson, S.P., and Choudhary, C. (2012). Proteomic investigations reveal a role for RNA processing factor THRAP3 in the DNA damage response. Mol. Cell *46*, 212–225.

Bermejo, R., Capra, T., Jossen, R., Colosio, A., Frattini, C., Carotenuto, W., Cocito, A., Doksani, Y., Klein, H., Gómez-González, B., et al. (2011). The replication checkpoint protects fork stability by releasing transcribed genes from nuclear pores. Cell *146*, 233–246.

Berti, M., and Vindigni, A. (2016). Replication stress: Getting back on track. Nat. Struct. Mol. Biol. *23*, 103–109.

Berti, M., Ray Chaudhuri, A., Thangavel, S., Gomathinayagam, S., Kenig, S., Vujanovic, M., Odreman, F., Glatter, T., Graziano, S., Mendoza-Maldonado, R., et al. (2013). Human RECQ1 promotes restart of replication forks reversed by DNA topoisomerase I inhibition. Nat. Struct. Mol. Biol. *20*, 347–354.

Blasius, M., Forment, J.V., Thakkar, N., Wagner, S.A., Choudhary, C., and Jackson, S.P. (2011). A phospho-proteomic screen identifies substrates of the checkpoint kinase Chk1. Genome Biol. *12*, R78.

Buisson, R., Boisvert, J.L., Benes, C.H., and Zou, L. (2015). Distinct but concerted roles of ATR, DNA-PK, and Chk1 in countering replication stress during S phase. Mol. Cell *59*, 1011–1024.

Buisson, R., Niraj, J., Rodrigue, A., Ho, C.K., Kreuzer, J., Foo, T.K., Hardy, E.J.L., Dellaire, G., Haas, W., Xia, B., et al. (2017). Coupling of homologous recombination and the checkpoint by ATR. Mol. Cell *65*, 336–346.

Chan, S.L., Huppertz, I., Yao, C., Weng, L., Moresco, J.J., Yates, J.R., 3rd, Ule, J., Manley, J.L., and Shi, Y. (2014). CPSF30 and Wdr33 directly bind to AAUAAA in mammalian mRNA 3′ processing. Genes Dev. *28*, 2370–2380.

Chen, L., Chen, J.Y., Zhang, X., Gu, Y., Xiao, R., Shao, C., Tang, P., Qian, H., Luo, D., Li, H., et al. (2017). R-ChIP using inactive RNase H reveals dynamic coupling of R-loops with transcriptional pausing at gene promoters. Mol. Cell *68*, 745–757.

Clerici, M., Faini, M., Aebersold, R., and Jinek, M. (2017). Structural insights into the assembly and polyA signal recognition mechanism of the human CPSF complex. eLife *6*. Published online December 23, 2017. https://doi.org/10.7554/eLife.33111.

Cohen, S., Puget, N., Lin, Y.L., Clouaire, T., Aguirrebengoa, M., Rocher, V., Pasero, P., Canitrot, Y., and Legube, G. (2018). Senataxin resolves RNA:DNA hybrids forming at DNA double-strand breaks to prevent translocations. Nat. Commun. *9*. Published online February 7, 2018. https://www.nature.com/articles/s41467-018-02894-w.

Cortez, D. (2015). Preventing replication fork collapse to maintain genome integrity. DNA Repair (Amst.) *32*, 149–157.

D'Alessandro, G., Adamowicz, M., Whelan, D., Howard, S.M., Jones-Weinert, C.W., Matti, V., Rothenberg, E., Cejka, P., and d'Adda di Fagagna, F. (2018). A role for RNA and DNA:RNA hybrids in the modulation of DNA repair by homologous recombination. bioRxiv. https://doi.org/10.1101/255976.

Davoli, T., Xu, A.W., Mengwasser, K.E., Sack, L.M., Yoon, J.C., Park, P.J., and Elledge, S.J. (2013). Cumulative haploinsufficiency and triplosensitivity drive aneuploidy patterns and shape the cancer genome. Cell *155*, 948–962.

Dobbelstein, M., and Sørensen, C.S. (2015). Exploiting replicative stress to treat cancer. Nat. Rev. Drug Discov. *14*, 405–423.

Domínguez-Sánchez, M.S., Barroso, S., Gómez-González, B., Luna, R., and Aguilera, A. (2011). Genome instability and transcription elongation impairment in human cells depleted of THO/TREX. PLoS Genet. *7*, e1002386.

Dungrawala, H., Rose, K.L., Bhat, K.P., Mohni, K.N., Glick, G.G., Couch, F.B., and Cortez, D. (2015). The replication checkpoint prevents two types of fork collapse without regulating replisome stability. Mol. Cell *59*, 998–1010.

Gaidatzis, D., Lerch, A., Hahne, F., and Stadler, M.B. (2015). QuasR: Quantification and annotation of short reads in R. Bioinformatics *31*, 1130–1132.

Gaillard, H., and Aguilera, A. (2016). Transcription as a threat to genome integrity. Annu. Rev. Biochem. *85*, 291–317.

García-Benítez, F., Gaillard, H., and Aguilera, A. (2017). Physical proximity of chromatin to nuclear pores prevents harmful R loop accumulation contributing to maintain genome stability. Proc. Natl. Acad. Sci. USA *114*, 10942–10947.

García-Muse, T., and Aguilera, A. (2016). Transcription-replication conflicts: How they occur and how they are resolved. Nat. Rev. Mol. Cell Biol. *17*, 553–563.

Hamperl, S., Bocek, M.J., Saldivar, J.C., Swigut, T., and Cimprich, K.A. (2017). Transcription-replication conflict orientation modulates R-loop levels and activates distinct DNA damage responses. Cell *170*, 774–786.

Hart, T., Chandrashekhar, M., Aregger, M., Steinhart, Z., Brown, K.R., MacLeod, G., Mis, M., Zimmermann, M., Fradet-Turcotte, A., Sun, S., et al. (2015). High-resolution CRISPR screens reveal fitness genes and genotype-specific cancer liabilities. Cell *163*, 1515–1526.

Hills, S.A., and Diffley, J.F. (2014). DNA replication and oncogene-induced replicative stress. Curr. Biol. *24*, R435–R444.

Janicki, S.M., Tsukamoto, T., Salghetti, S.E., Tansey, W.P., Sachidanandam, R., Prasanth, K.V., Ried, T., Shav-Tal, Y., Bertrand, E., Singer, R.H., and Spector, D.L. (2004). From silencing to gene expression: Real-time analysis in single cells. Cell *116*, 683–698.

Karnitz, L.M., and Zou, L. (2015). Molecular pathways: Targeting ATR in cancer therapy. Clin. Cancer Res. *21*, 4780–4785.

Kavanaugh, G., Ye, F., Mohni, K.N., Luzwick, J.W., Glick, G., and Cortez, D. (2015). A whole genome RNAi screen identifies replication stress response genes. DNA Repair (Amst.) *35*, 55–62.

Kumar, A., Mazzanti, M., Mistrik, M., Kosar, M., Beznoussenko, G.V., Mironov, A.A., Garrè, M., Parazzoli, D., Shivashankar, G.V., Scita, G., et al. (2014). ATR mediates a checkpoint at the nuclear envelope in response to mechanical stress. Cell *158*, 633–646.

Lawrence, M., Huber, W., Pagès, H., Aboyoun, P., Carlson, M., Gentleman, R., Morgan, M.T., and Carey, V.J. (2013). Software for computing and annotating genomic ranges. PLoS Comput. Biol. *9*, e1003118.

Lawrence, M.S., Stojanov, P., Mermel, C.H., Robinson, J.T., Garraway, L.A., Golub, T.R., Meyerson, M., Gabriel, S.B., Lander, E.S., and Getz, G. (2014). Discovery and saturation analysis of cancer genes across 21 tumour types. Nature *505*, 495–501.

Lecona, E., and Fernandez-Capetillo, O. (2018). Targeting ATR in cancer. Nat. Rev. Cancer *18*, 586–595.

Lemaître, C., Grabarz, A., Tsouroula, K., Andronov, L., Furst, A., Pankotai, T., Heyer, V., Rogier, M., Attwood, K.M., Kessler, P., et al. (2014). Nuclear position dictates DNA repair pathway choice. Genes Dev. *28*, 2450–2463.

Lu, W.T., Hawley, B.R., Skalka, G.L., Baldock, R.A., Smith, E.M., Bader, A.S., Malewicz, M., Watts, F.Z., Wilczynska, A., and Bushell, M. (2018). Drosha drives the formation of DNA:RNA hybrids around DNA break sites to facilitate DNA repair. Nat. Commun. *9*. Published online February 7, 2018. https://www.nature.com/articles/s41467-018-02893-x.

Lukas, C., Savic, V., Bekker-Jensen, S., Doil, C., Neumann, B., Pedersen, R.S., Grøfte, M., Chan, K.L., Hickson, I.D., Bartek, J., and Lukas, J. (2011). 53BP1 nuclear bodies form around DNA lesions generated by mitotic transmission of chromosomes under replication stress. Nat. Cell Biol. *13*, 243–253.

Macheret, M., and Halazonetis, T.D. (2015). DNA replication stress as a hallmark of cancer. Annu. Rev. Pathol. *10*, 425–448.

Matsuoka, S., Ballif, B.A., Smogorzewska, A., McDonald, E.R., 3rd, Hurov, K.E., Luo, J., Bakalarski, C.E., Zhao, Z., Solimini, N., Lerenthal, Y., et al. (2007). ATM and ATR substrate analysis reveals extensive protein networks responsive to DNA damage. Science *316*, 1160–1166.

Michelena, J., Lezaja, A., Teloni, F., Schmid, T., Imhof, R., and Altmeyer, M. (2018). Analysis of PARP inhibitor toxicity by multidimensional fluorescence microscopy reveals mechanisms of sensitivity and resistance. Nat. Commun. *9*, 2678.

Michelini, F., Pitchiaya, S., Vitelli, V., Sharma, S., Gioia, U., Pessina, F., Cabrini, M., Wang, Y., Capozzo, I., Iannelli, F., et al. (2017). Damage-induced lncRNAs control the DNA damage response through interaction with DDRNAs at individual double-strand breaks. Nat. Cell Biol. *19*, 1400–1411.

Nguyen, H.D., Yadav, T., Giri, S., Saez, B., Graubert, T.A., and Zou, L. (2017). Functions of replication protein A as a sensor of R loops and a regulator of RNaseH1. Mol. Cell *65*, 832–847.e4.

Nijhawan, D., Zack, T.I., Ren, Y., Strickland, M.R., Lamothe, R., Schumacher, S.E., Tsherniak, A., Besche, H.C., Rosenbluh, J., Shehata, S., et al. (2012). Cancer vulnerabilities unveiled by genomic loss. Cell *150*, 842–854.

O'Connor, M.J. (2015). Targeting the DNA damage response in cancer. Mol. Cell *60*, 547–560.

Pasero, P., and Vindigni, A. (2017). Nucleases acting at stalled forks: How to reboot the replication program with a few shortcuts. Annu. Rev. Genet. *51*, 477–499.

Paulsen, R.D., Soni, D.V., Wollman, R., Hahn, A.T., Yee, M.C., Guan, A., Hesley, J.A., Miller, S.C., Cromwell, E.F., Solow-Cordero, D.E., et al. (2009). A genome-wide siRNA screen reveals diverse cellular processes and pathways that mediate genome stability. Mol. Cell *35*, 228–239.

Poli, J., Gerhold, C.B., Tosi, A., Hustedt, N., Seeber, A., Sack, R., Herzog, F., Pasero, P., Shimada, K., Hopfner, K.P., and Gasser, S.M. (2016). Mec1, INO80, and the PAF1 complex cooperate to limit transcription replication conflicts through RNAPII removal during replication stress. Genes Dev. *30*, 337–354.

Reddy, K.L., Zullo, J.M., Bertolino, E., and Singh, H. (2008). Transcriptional repression mediated by repositioning of genes to the nuclear lamina. Nature *452*, 243–247.

Salas-Armenteros, I., Pérez-Calero, C., Bayona-Feliu, A., Tumini, E., Luna, R., and Aguilera, A. (2017). Human THO-Sin3A interaction reveals new mechanisms to prevent R-loops that cause genome instability. EMBO J. *36*, 3532–3547.

Saldivar, J.C., Cortez, D., and Cimprich, K.A. (2017). The essential kinase ATR: Ensuring faithful duplication of a challenging genome. Nat. Rev. Mol. Cell Biol. *18*, 622–636.

Saldivar, J.C., Hamperl, S., Bocek, M.J., Chung, M., Bass, T.E., Cisneros-Soberanis, F., Samejima, K., Xie, L., Paulson, J.R., Earnshaw, W.C., et al. (2018). An intrinsic S/G_2 checkpoint enforced by ATR. Science *361*, 806–810.

Schindelin, J., Arganda-Carreras, I., Frise, E., Kaynig, V., Longair, M., Pietzsch, T., Preibisch, S., Rueden, C., Saalfeld, S., Schmid, B., et al. (2012). Fiji: An open-source platform for biological-image analysis. Nat. Methods *9*, 676–682.

Schlacher, K., Christ, N., Siaud, N., Egashira, A., Wu, H., and Jasin, M. (2011). Double-strand break repair-independent role for BRCA2 in blocking stalled replication fork degradation by MRE11. Cell *145*, 529–542.

Schönemann, L., Kühn, U., Martin, G., Schäfer, P., Gruber, A.R., Keller, W., Zavolan, M., and Wahle, E. (2014). Reconstitution of CPSF active in polyadenylation: Recognition of the polyadenylation signal by WDR33. Genes Dev. *28*, 2381–2393.

Shanbhag, N.M., Rafalska-Metcalf, I.U., Balane-Bolivar, C., Janicki, S.M., and Greenberg, R.A. (2010). ATM-dependent chromatin changes silence transcription in cis to DNA double-strand breaks. Cell *141*, 970–981.

Sollier, J., and Cimprich, K.A. (2015). Breaking bad: R-loops and genome integrity. Trends Cell Biol. *25*, 514–522.

Sollier, J., Stork, C.T., García-Rubio, M.L., Paulsen, R.D., Aguilera, A., and Cimprich, K.A. (2014). Transcription-coupled nucleotide excision repair factors promote R-loop-induced genome instability. Mol. Cell *56*, 777–785.

Suzuki, Y., Holmes, J.B., Cerritelli, S.M., Sakhuja, K., Minczuk, M., Holt, I.J., and Crouch, R.J. (2010). An upstream open reading frame and the context of the two AUG codons affect the abundance of mitochondrial and nuclear RNase H1. Mol. Cell. Biol. *30*, 5123–5134.

Tang, J., Cho, N.W., Cui, G., Manion, E.M., Shanbhag, N.M., Botuyan, M.V., Mer, G., and Greenberg, R.A. (2013). Acetylation limits 53BP1 association with damaged chromatin to promote homologous recombination. Nat. Struct. Mol. Biol. *20*, 317–325.

Técher, H., Koundrioukoff, S., Nicolas, A., and Debatisse, M. (2017). The impact of replication stress on replication dynamics and DNA damage in vertebrate cells. Nat. Rev. Genet. *18*, 535–550.

Toledo, L.I., Altmeyer, M., Rask, M.B., Lukas, C., Larsen, D.H., Povlsen, L.K., Bekker-Jensen, S., Mailand, N., Bartek, J., and Lukas, J. (2013). ATR prohibits replication catastrophe by preventing global exhaustion of RPA. Cell *155*, 1088–1103.

Tresini, M., Warmerdam, D.O., Kolovos, P., Snijder, L., Vrouwe, M.G., Demmers, J.A.A., van IJcken, W.F.J., Grosveld, F.G., Medema, R.H., Hoeijmakers, J.H.J., et al. (2015). The core spliceosome as target and effector of non-canonical ATM signalling. Nature *523*, 53–58.

Wang, T., Birsoy, K., Hughes, N.W., Krupczak, K.M., Post, Y., Wei, J.J., Lander, E.S., and Sabatini, D.M. (2015). Identification and characterization of essential genes in the human genome. Science *350*, 1096–1101.

Yazinski, S.A., and Zou, L. (2016). Functions, regulation, and therapeutic implications of the ATR checkpoint pathway. Annu. Rev. Genet. *50*, 155–173.

Zack, T.I., Schumacher, S.E., Carter, S.L., Cherniack, A.D., Saksena, G., Tabak, B., Lawrence, M.S., Zhsng, C.Z., Wala, J., Mermel, C.H., et al. (2013). Pan-cancer patterns of somatic copy number alteration. Nat. Genet. *45*, 1134–1140.

Zeman, M.K., and Cimprich, K.A. (2014). Causes and consequences of replication stress. Nat. Cell Biol. *16*, 2–9.

STAR★METHODS

KEY RESOURCES TABLE

REAGENT or RESOURCE	SOURCE	IDENTIFIER
Antibodies		
H2AX Phospho S139 primary antibody (mouse)	Biolegend	Cat# 613401; RRID: AB_315794
CHK1 Phospho S317 primary antibody (rabbit)	Cell Signaling	Cat# 2344; RRID: AB_331488
CHK1 Phospho S345 primary antibody (rabbit)	Cell Signaling	Cat# 2348; RRID: AB_331212
KAP1 phospho S824 primary antibody (rabbit)	Abcam	Cat# ab70369; RRID: AB_1209417
KAP1 primary antibody (rabbit)	Bethyl	Cat# A300-274A; RRID: AB_185559
RPA32 Phospho S4/8 primary antibody (rabbit)	Bethyl	Cat# A300-245A; RRID: AB_210547
RPA32 primary antibody (mouse)	Abcam	Cat# ab2175; RRID: AB_302873
RPA70 primary antibody (rabbit)	Abcam	Cat# ab79398; RRID: AB_1603759
53BP1 primary antibody (rabbit)	Santa-Cruz	Cat# sc-22760; RRID: AB_2256326
PCNA primary antibody (mouse)	Santa-Cruz	Cat# sc-56; RRID: AB_628110
GAPDH primary antibody (mouse)	Merck	Cat# MAB374; RRID: AB_2107445
Cyclin A primary antibody (rabbit)	Santa-Cruz	Cat# sc-751; RRID: AB_631329
Cyclin A primary antibody (mouse)	Abcam	Cat# ab16726; RRID: AB_302478
WDR33 primary antibody (rabbit)	Novus Biologicals	Cat# NB100-58831; RRID: AB_2288472
THOC1 primary antibody (mouse)	Santa-Cruz	Cat# sc-136426; RRID: AB_10610671
RNA Pol II primary antibody (mouse)	Active Motif	Cat# 39097; RRID: AB_2732926
RNA Pol II pS2 CTD primary antibody (rabbit)	Abcam	Cat# ab5095; RRID: AB_304749
S9.6 primary antibody (mouse)	Kerafast	Cat# ENH001; RRID: AB_2687463
Tubulin primary antibody (mouse)	Sigma-Aldrich	Cat# T6199; RRID: AB_477583
Histone H3 primary antibody (rabbit)	Abcam	Cat# ab1791; RRID: AB_302613
Lamin B1 primary antibody (rabbit)	Abcam	Cat# ab16048; RRID: AB_443298
BrdU primary antibody (mouse)	BD Biosciences	Cat# 347580; RRID: AB_400326
GFP primary antibody (rabbit)	Torrey Pines Biolabs	Cat# TP401 071519; RRID: AB_10013661
CldU primary antibody (rat)	Abcam	Cat# ab6326; RRID: AB_305426
IgG primary antibody (rabbit)	Santa-Cruz	Cat# sc-2027; RRID: AB_737197
Aquarius primary antibody (rabbit)	ProteinTech	Cat# 24342-1-AP
Alexa Fluor 488 goat-anti-Mouse	ThermoFisher	Cat# A-11029; RRID: AB_2534088
Alexa Fluor 488 goat-anti-Rabbit	ThermoFisher	Cat# A-11034; RRID: AB_2576217
Alexa Fluor 568 goat-anti-Mouse	ThermoFisher	Cat# A-11031; RRID: AB_144696
Alexa Fluor 568 goat-anti-Rabbit	ThermoFisher	Cat# A-11036; RRID: AB_10563566
Alexa Fluor 647 goat-anti-Mouse	ThermoFisher	Cat# A-21235; RRID: AB_2535804
Alexa Fluor 647 goat-anti-Rabbit	ThermoFisher	Cat# A-21244; RRID: AB_2535812
Cy3 AffiniPure Donkey Anti-Rat	Jackson Immuno	Cat# 712-166-153; RRID: AB_2340669
Anti-Mouse IgG (H+L), Peroxidase	AdipoGen Life Science	Cat# VC-PI-2000-M001
Anti-Rabbit IgG (H+L), Peroxidase	AdipoGen Life Science	Cat# VC-PI-1000-M001
Bacterial and Virus Strains		
Library Efficiency DH5α Competent Cells	ThermoFisher	Cat# 18263012
Chemicals, Peptides, and Recombinant Proteins		
Q5 High-Fidelity DNA polymerase	New England Biolabs	Cat# M0491S
T5 Exonuclease	New England Biolabs	Cat# M0363S
Taq DNA ligase	New England Biolabs	Cat# M0208S
Phusion High-Fidelity polymerase	New England Biolabs	Cat# M0530S
NAD	AppliChem	Cat# A1124

(*Continued on next page*)

Continued

REAGENT or RESOURCE	SOURCE	IDENTIFIER
dATP	Sigma-Aldrich	Cat# D4788
dCTP	Sigma-Aldrich	Cat# D4913
dGTP	Sigma-Aldrich	Cat# D5038
dTTP	Sigma-Aldrich	Cat# 11969048001
Dulbecco's modified Eagle's medium (DMEM)	ThermoFisher	Cat# 61965-026
Tet system approved fetal bovine serum	Clontech	Cat# 631107
Penicillin-streptomycin	ThermoFisher	Cat# 15140-122
Puromycin	InvivoGen	Cat# ant-pr-1
Hygromycin B	ThermoFisher	Cat# 10687010
Geneticin (G418 sulfate)	ThermoFisher	Cat# 10131027
Gentamicin	Sigma-Aldrich	Cat# G1397
OptiMEM	ThermoFisher	Cat# 31985070
TransIT-LT1	Mirus	Cat# MIR 2300
5-bromo-2-deoxyuridine (BrdU)	Sigma-Aldrich	Cat# B5002
ATRi Az-20	Tocris	Cat# 5198
ATRi VE-821	Selleckchem	Cat# S8007
Camptothecin	Selleckchem	Cat# S1288
Roscovitine	Selleckchem	Cat# S1153
Olaparib	Selleckchem	Cat# S1060
DRB	Sigma-Aldrich	Cat# D1916
Flavopiridol	Selleckchem	Cat# S1230
AZD5438	Selleckchem	Cat# S2621
Hydroxyurea	Sigma-Aldrich	Cat# H8627
Doxycycline	Sigma-Aldrich	Cat# D9891
CDC7i PHA-767491	Selleckchem	Cat# S2742
Aphidicolin	Sigma-Aldrich	Cat# A0781
Diospyrin D	Dr. Pavel Janscak	N/A
TRIzol reagent	ThermoFisher	Cat# 15596026
Random hexamers	Roche	Cat# 11034731001
Protease inhibitor cocktail cOmplete	Roche	Cat# 11873580001
S7 Nuclease	Sigma-Aldrich	Cat# 10107921001
Proteinase K	Roche	Cat# 3115836001
Benzonase	Merck	Cat# 71206-3
RnaseA	Roche	Cat# 10109169001
Methanol-free formaldehyde 16% (w/v)	ThermoFisher	Cat# 28908
Glycine	Sigma-Aldrich	Cat# G8898
Dynabeads Protein A	ThermoFisher	Cat# 10001D
Dynabeads Protein G	ThermoFisher	Cat# 10003D
Protein G Sepharose 4 Fast Flow	GE Healthcare	Cat# 17-0618-01
Ribonucleic acid, transfer from baker's yeast	Sigma-Aldrich	Cat# R5636
Bovine Serum Albumin	Sigma-Aldrich	Cat# A9418
Formamide	Sigma-Aldrich	Cat# 47671
Yeast tRNA	ThermoFisher	Cat# 15401011
DAPI	ThermoFisher	Cat# D1306
Mowiol 4.88	Calbiochem	Cat# 475904
Critical Commercial Assays		
QuikChange Site-Directed Mutagenesis kit	Agilent Technologies	Cat# 210515
TransIT-LT1 transfection reagent	Mirus Bio	Cat# MIR 2300

(*Continued on next page*)

Continued

REAGENT or RESOURCE	SOURCE	IDENTIFIER
5-ethynyl-2′-desoxyuridine (EdU) labeling kit	ThermoFisher	Cat# C10337
5-Ethynyl Uridine (EU) labeling kit	ThermoFisher	Cat# C10329
MultiScribe Reverse Transcriptase	ThermoFisher	Cat# 4311235
KAPA Biosystems Sybr Fast qPCR Kit	Roche	Cat# KK4600
Lipofectamine RNAiMAX	ThermoFisher	Cat# 13778-150
HiPerFect Transfection Reagent	QIAGEN	Cat# 301705
QIAGEN MinElute PCR Purification Kit	QIAGEN	Cat# 28004
NEBNext ChIP-Seq Library Prep Master Mix Set for Illumina	New England Bio Labs	Cat# E6240
NEBNext Multiplex Oligos for Illumina (Index Primers Set 1)	New England Bio Labs	Cat# E7335
NucleoSpin PCR Clean-Up	MACHEREY-NAGEL GmbH & Co. KG	Cat# 740609
Stellaris FISH Probes, Human ACTB with Quasar 670 Dye	LGC Biosearch Technologies	Cat# VSMF-2003-5
Stellaris FISH Probes, Human ACTB_intron with Quasar 570 Dye	LGC Biosearch Technologies	Cat# ISMF-2002-5
Deposited Data		
RNA Pol II pS2 ChIP-Seq results	This paper	https://www.ncbi.nlm.nih.gov/geo/query/acc.cgi?acc=GSE118795
Additional unprocessed datasets on Mendeley	This paper	https://doi.org/10.17632/3p6bvgb5ys.1
Experimental Models: Cell Lines		
U-2 OS cells (female origin, STR authenticated)	ATCC	Cat# HTB-96; RRID:CVCL_0042
hTERT-RPE1 cells (female origin)	ATCC	Cat# CRL-4000; RRID:CVCL_4388
HeLa cells (female origin)	ATCC	Cat# CCL-2; RRID:CVCL_0030
U-2 OS cells harboring 256x lac operator sequence+ER-mCherry-LacI-FokI	Tang et al., 2013	N/A
U-2 OS derived 2-6-3 rtTA+YFP-MS2 cells	Shanbhag et al., 2010	N/A
I-U2OS19 ptight13 GFP-LacI	Lemaître et al., 2014	N/A
I-U2OS19 ptight13 GFP-LacI-ΔEMD	Lemaître et al., 2014	N/A
U-2 OS GFP-WDR33 siRNA-sensitive	This paper	N/A
U-2 OS GFP-WDR33 siRNA-resistant	This paper	N/A
U-2 OS T-REx GFP-RNaseH1 WT	This paper	N/A
U-2 OS T-REx GFP-RNaseH1 D210N	This paper	N/A
Oligonucleotides		
Cloning primer: pAcGFP_lin_fwd: GATCATAATCAGCCATACCACATTTGTAGAGG	This paper	N/A
Cloning primer: pAcGFP_lin_rev: TCGAGATCTGAGTCCGGAC	This paper	N/A
Cloning primer: WDR33p1_to_pAc_fwd: CTGTACAAGTCCGGACTCAGATCTCGAATGGCTACAGAAATTGGTTCTCC	This paper	N/A
Cloning primer: WDR33p1_to_p3_rev: CTGGAGGGTGAGGTCCTCTCATCTCTTGtttatcacctggtcgg	This paper	N/A
Cloning primer: WDR33p1_to_p2_rev: caggtaaaaggtttagattatatcgatctcgcattttatcacctggtcgg	This paper	N/A
Cloning primer: WDR33p2_fwd: tgcgagatcgatataatctaaacctttacc	This paper	N/A
Cloning primer: WDR33p2_rev: CTGGAGGGTGAGGTCC	This paper	N/A
Cloning primer: WDR33p3_to_p2_fwd: caagagatgagaggacctcaccctccaggtggactactgggacacg	This paper	N/A
Cloning primer: WDR33p3_to_pAc_rev: CTACAAATGTGGTATGGCTGATTATGATCctaccgaccccttccaccacc	This paper	N/A

(*Continued on next page*)

Continued

REAGENT or RESOURCE	SOURCE	IDENTIFIER
Cloning primer: WDR33_siRes: GATGTTCCAGGCACACA AAGAAGCTATTAGAGAGGCCAG	This paper	N/A
Cloning primer: RNH1-F(D210N): CTGGTTCTGTATACAAA CAGTATGTTTACGA	This paper	N/A
Cloning primer: RNH1-R(D210N): TCGTAAACATACTGTTT GTATACAGAACCAG	This paper	N/A
Cloning primer: RNH1 sh730F: GATCTACGATAAATGGTA TAACTAACCTCGAGGTTAGTTATACCATTTATCGTTTTTT CTGCAGA	This paper	N/A
Cloning primer: RNH1 sh730R: AGCTTCTGCAGAAAAAA CGATAAATGGTATAACTAACCTCGAGGTTAGTTATACC ATTTATCGTA	This paper	N/A
Cloning primer: RNH1_MTG730_1F: CAGACAGTATGTTTA CCATCAACGGCATAACTAACTGGGTTCAAGG	This paper	N/A
Cloning primer: RNH1_MTG730_1R: CCTTGAACCCAGTTA GTTATGCCGTTGATGGTAAACATACTGTCTG	This paper	N/A
Cloning primer: RNH1_MTG730_2F: GTTTACCATCAACG GCATCACGAATTGGGTTCAAGGTTGG	This paper	N/A
Cloning primer: RNH1_MTG730_2R: CCAACCTTGAACCCA ATTCGTGATGCCGTTGATGGTAAAC	This paper	N/A
qRT-PCR primer: hWDR33 Forward: TAGGTGGACTCCAG AAGGAA	This paper	N/A
qRT-PCR primer: hWDR33 Reverse: GCTGTCGTGAGCCT GTAATA	This paper	N/A
qRT-PCR primer: hCPSF30 Forward: AAATTCATGCACCC TCGATTTG	This paper	N/A
qRT-PCR primer: hCPSF30 Reverse: AAGGAGGACGACC TTTGTAATG	This paper	N/A
qRT-PCR primer: hFIP1 Forward: CACCACAGTATGGGA GTTATGG	This paper	N/A
qRT-PCR primer: hFIP1 Reverse: CAGGTGCATCAAGGT CTACTC	This paper	N/A
qRT-PCR primer: hCPSF160 Forward: TTCAAGGATGCC AAGCTGTC	This paper	N/A
qRT-PCR primer: hCPSF160 Reverse: AGCTCAGGCTCCT CAAAGTA	This paper	N/A
qRT-PCR primer: hTHOC1 Forward: GGTCAGAAGCACAC TGAAGATAG	This paper	N/A
qRT-PCR primer: hTHOC1 Reverse: GGAATAGAGCACGT TGTTGGA	This paper	N/A
qRT-PCR primer: hTHOC2 Forward: GTTCCCGCAGAGTG GATAAA	This paper	N/A
qRT-PCR primer: hTHOC2 Reverse: AGCTTGCTGGAAAT CTCTGTAT	This paper	N/A
qRT-PCR primer: hRNaseH1 Forward: TCAGTGGATGCAT GTTCCTG	This paper	N/A
qRT-PCR primer: hRNaseH1 Reverse: GGCTCAGTCTTC CGATTGTT	This paper	N/A
qRT-PCR primer: hGAPDH Forward: GCTGCGGGAGGCG TGTGTG	This paper	N/A
qRT-PCR primer: hGAPDH Reverse: CTCCTTGCGGGGAA CAGCTACC	This paper	N/A

(*Continued on next page*)

Continued

REAGENT or RESOURCE	SOURCE	IDENTIFIER
qRT-PCR primer: hRPS12 Forward: GGAGGCTTGGGTG CGTTC	This paper	N/A
qRT-PCR primer: hRPS12 Reverse: GGTGGCAGTTTTG TTCCG	This paper	N/A
FISH probe: Lac operator: AATTGTTATCCGCTCAC	This paper	N/A
poly(A) FISH probe: 5′ Cy3-oligo(dT)40	This paper	N/A
SilencerSelect siRNA against WDR33 #71	ThermoFisher	Cat# ID s30771
SilencerSelect siRNA against WDR33 #72	ThermoFisher	Cat# ID s30772
SilencerSelect siRNA against WDR33 #73	ThermoFisher	Cat# ID s30773
Mission esiRNA against WDR33	Sigma-Aldrich	Cat# ID HU-11890-1
FlexiTube siRNA against WDR33	QIAGEN	Cat# ID HS_WDR33_5
SilencerSelect siRNA against CPSF30	ThermoFisher	Cat# ID s21412
SilencerSelect siRNA against CPSF160	ThermoFisher	Cat# ID s26658
SilencerSelect siRNA against FIP1	ThermoFisher	Cat# ID s37692
SilencerSelect siRNA against CDC45	ThermoFisher	Cat# ID s15831
SilencerSelect siRNA against BRCA2	ThermoFisher	Cat# ID s2085
siRNA against RPA1	ThermoFisher	Cat# ID 142498
siRNA against THOC1 #1: CAGAUUGAGUGUGACAGUGA AdTdT	QIAGEN	N/A
SilencerSelect siRNA against THOC1 #2	ThermoFisher	Cat# ID s19395
SilencerSelect siRNA against THOC2 #1	ThermoFisher	Cat# ID s32861
SilencerSelect siRNA against THOC2 #2	ThermoFisher	Cat# ID s32862
SilencerSelect siRNA against ENY2	ThermoFisher	Cat# ID s32449
SilencerSelect siRNA against TPR	ThermoFisher	Cat# ID s14353
SilencerSelect siRNA against NUP153	ThermoFisher	Cat# ID s19374
SilencerSelect siRNA against Aquarius	ThermoFisher	Cat# ID s18727
SilencerSelect negative control siRNA siNeg1	ThermoFisher	Cat# 4390843
SilencerSelect negative control siRNA siNeg2	ThermoFisher	Cat# 4390846
QIAGEN negative control siRNA	QIAGEN	Cat# 1022076
Microsynth custom designed negative control siRNA: UUC UCCGAACGU GUCACGUUUdTdT	Microsynth	N/A
Recombinant DNA		
pAcGFP-C1 hWDR33 siRNA-sensitive	This paper	N/A
pAcGFP-C1 hWDR33 siRNA-resistant	This paper	N/A
pAIO hM27RNaseH1-EGFP WT	This paper	N/A
pAIO hM27RNaseH1-EGFP D210N	This paper	N/A
Software and Algorithms		
GraphPad Prism 7.0	GraphPad Software	https://www.graphpad.com/
Olympus ScanR Image Analysis Software 3.0.0	Olympus	https://www.olympus-lifescience.com/de/microscopes/inverted/scanr/#!
TIBCO Spotfire 7.0.1	TIBCO Software	https://www.tibco.com/products/tibco-spotfire
Fiji 2.0.0	Schindelin et al., 2012	https://fiji.sc/
Trim Galore	Bioinformatics Group at the Babraham Institute	https://www.bioinformatics.babraham.ac.uk/projects/trim_galore/
QuasR	Gaidatzis et al., 2015	https://bioconductor.org/packages/release/bioc/html/QuasR.html
GenomicRanges	Lawrence et al., 2013	https://github.com/Bioconductor/GenomicRanges

CONTACT FOR REAGENTS AND RESOURCE SHARING

Further information and requests for resources and reagents should be directed to and will be fulfilled by the Lead Contact, Matthias Altmeyer (matthias.altmeyer@uzh.ch).

EXPERIMENTAL MODEL AND SUBJECT DETAILS

Cell lines

All cells were grown in a sterile cell culture environment and routinely tested for mycoplasma contamination by PCR. Human U-2 OS cells, hTERT-RPE1 cells, and HeLa cells (all of female origin) were grown under standard cell culture conditions (humidified atmosphere, 5% CO_2) in Dulbecco's modified Eagle's medium (DMEM) containing 10% fetal bovine serum (GIBCO) and penicillin-streptomycin antibiotics.

Human U-2 OS T-REx-derived clones for the inducible expression of GFP-RNaseH1 or catalytically inactive GFP-RNaseH1 D210N were grown under standard cell culture conditions in DMEM containing 10% Tet system approved fetal bovine serum (Takara), with penicillin-streptomycin, 1 μg/mL puromycin and 50 μg/mL hygromycin antibiotics. Addition of doxycycline (1 ng/mL, Sigma) for 24 hr was used to induce expression.

U-2 OS cells harboring an array of the lac operator sequence and stably expressing ER-mCherry-LacI-FokI (Tang et al., 2013) were grown under standard cell culture conditions (humidified atmosphere, 5% CO_2) in Dulbecco's modified Eagle's medium (DMEM) containing 10% fetal bovine serum (GIBCO) and penicillin-streptomycin antibiotics. Transient transfection of mCherry-tagged LacI allowed for the visualization of the lac operator array in the absence of FokI induction and without FokI-induced DNA damage.

U-2 OS 2-6-3 rtTA+YFP-MS2 reporter cells containing an array of the lac operator sequence and 24 copies of the MS2 sequence and stably expressing YFP-MS2 protein (Shanbhag et al., 2010) were grown under standard cell culture conditions (humidified atmosphere, 5% CO_2) in Dulbecco's modified Eagle's medium (DMEM) containing 10% fetal bovine serum (GIBCO) and penicillin-streptomycin antibiotics, in the presence of 100 μg/mL hygromycin and 400 μg/mL G418, both of which were added freshly at each passage. Nascent transcripts emerging from the stably integrated array were monitored through YFP-MS2 binding 4 hr after addition of 1 μg/mL doxycycline (D9891, Sigma).

I-U2OS19 ptight13 GFP-LacI and GFP-LacI-ΔEMD cells harboring a stably integrated I-SceI restriction site flanked by an array of the lac operator sequence (Lemaître et al., 2014) were cultured under standard cell culture conditions (humidified atmosphere, 5% CO_2) in Dulbecco's modified Eagle's medium (DMEM) containing 10% fetal bovine serum (GIBCO) and penicillin-streptomycin antibiotics in the presence of 800 μg/mL G418, 40 μg/mL gentamicine and 2 mM IPTG (inhibitor of the LacI-LacO interaction). Removal of IPTG for 16 hr enabled the visualization of the LacO locus and assessing its nuclear localization without I-SceI-mediated break induction.

All cultured cells were routinely assessed by quantitative image-based cytometry (QIBC) for proper proliferation and absence of abnormal stress signals using cell cycle resolved profiles of γH2AX, CyclinA, CyclinB, 53BP1 and RPA foci, as well as nuclear morphology and EdU incorporation as readouts.

Bacterial strains

Cloning was done using chemically competent bacteria generated in-house, derived from Library Efficiency DH5α Competent Cells (ThermoFisher).

METHOD DETAILS

pAcGFP-WDR33 cloning

To facilitate the cloning of full-length human WDR33 into a mammalian expression vector, the WDR33 cDNA (Schönemann et al., 2014) was first split into 3 smaller segments for PCR-based amplification: part 1 from bp 1-1230, part 2 from bp 1231-2449 and part 3 from bp 2450-4011. pAcGFP-C1 was linearized with Q5 DNA polymerase using primers pAcGFP_lin_fwd and pAcGFP_lin_rev. WDR33 parts 1 and 3 were amplified with Q5 DNA polymerase from a MultiBac plasmid using primers WDR33p1_to_pAc_fwd together with WDR33p1_to_p3_rev and WDR33p3_to_p2_fwd with WDR33p3_to_pAc_rev. The amplified products were DpnI digested and purified by gel extraction followed by isothermal Gibson assembly. The resulting pAcGFP-C1 with WDR33 parts 1+3 was linearized using WDR33p3_to_p2_fwd and WDR33p1_to_p2_rev. Part 2 was amplified with primers WDR33p2_fwd and WDR33p2_rev. The components were DpnI digested and purified by gel extraction followed by isothermal Gibson assembly to clone the full-length human WDR33. The pAcGFP-C1-WDR33 wild-type construct was rendered siRNA-resistant to the SilencerSelect WDR33 siRNA s30772 by using the QuikChange lightning multi-site directed mutagenesis kit with the primer WDR33_siRes according to the manufacturer's instructions. All constructs were confirmed by sequencing. Primer sequences are provided in the Key Resources Table.

Generation of GFP-WDR33 cell lines

50'000 U-2 OS cells were seeded into two wells of a 6-well plate. On the following day, cells were transfected with 2 μg plasmid DNA in 250μL OptiMEM using 6 μL TransIT-LT1. Cells were selected for the subsequent 2 weeks with 400 μg/mL G418 until a polyclonal cell population was obtained with a sub-population of cells stably expressing either siRNA-sensitive or siRNA-resistant GFP-WDR33. 2′000 cells from each population were then seeded into a 15cm dish followed by continued selection with G418. After 2 weeks of colony growth, individual colonies were picked with cloning cylinders, expanded further, and screened for pAcGFP-C1-WDR33 expression and monoclonality using QIBC.

Generation of GFP-RNaseH1 cell lines

U-2 OS T-REx cells were stably transfected with pAIO-based constructs of GFP-RNaseH1 or catalytically inactive GFP-RNaseH1(D210N) and selected in the presence of 1 μg/mL puromycin. The plasmid for GFP-hM27RNaseH1, lacking the amino-terminal mitochondrial localization sequence, was kindly provided by Dr. Robert Crouch (Suzuki et al., 2010). A point mutation in the catalytic site D210N was introduced using the QuikChange Site-Directed Mutagenesis kit (Agilent Technologies). The EcoRI-NotI fragment of plasmid pEGFP-N2 containing hM27RNaseH1 (WT or D210N) was blunt ended and sub-cloned into pAIO digested with EcoRV. The correct orientation of the insert was confirmed by control digestion. A DNA oligoduplex encoding for an shRNA for endogenous RNaseH1 silencing targeted to nucleotides 730-751 was introduced between the BglII and HindIII sites of pAIO. The NotI-HindIII fragment of pAIO shRNaseH1 containing shRNA was ligated with the HindIII-NotI fragment of pAIO containing hM27RNaseH1-EGFP. In the resulting construct seven silent mutations were introduced into the RNaseH1 cDNA between nucleotides 730-751 by two rounds of mutagenesis to render the RNaseH1 transcript resistant to the shRNA. All primer sequences are provided in the Key Resources Table.

EdU/EU labeling and BrdU incorporation

For pulsed EdU (5-ethynyl-2′-desoxyuridine, Thermo Fisher Scientific) incorporation, cells were incubated for 20 min in medium containing 10 μM EdU. The Click-iT EdU Alexa Fluor Imaging Kit (Thermo Fisher Scientific) was used for EdU detection. For pulsed EU (5-Ethynyl Uridine, Thermo Fisher Scientific) incorporation, cells were incubated for 1 hr in medium containing 0.5 mM EU. The Click-iT EU Alexa Fluor Imaging Kit (Thermo Fisher Scientific) was used for EU detection. For detection of single stranded DNA, cells were incubated with 10 μM 5-bromo-2-deoxyuridine (BrdU, Sigma) for 24 hr and BrdU was detected under native, non-denaturing conditions.

Drug treatments

Unless stated otherwise the following compounds were used in this manuscript at the indicated final concentrations: ATRi Az-20 (1 μM, 5198, Tocris), ATRi VE-821 (10 μM, S8007, Selleckchem), Camptothecin (50 nM, S1288, Selleckchem), Roscovitine (20 μM, S1153, Selleckchem), Olaparib (10 μl, S1060, Selleckchem), DRB (100 μM, D1916, Sigma), Flavopiridol (1.25 μM, S1230, Selleckchem), AZD5438 (1 μM, S2621, Selleckchem), Hydroxyurea (HU, 2 mM, H8627, Sigma), Doxycycline (1-1000 ng/mL, D9891, Sigma), CDC7i (25 μM, S2742, Selleckchem), Aphidicolin (0.2 μM, A0781, Sigma), Diospyrin D (10 μM, gift of Dr. Pavel Janscak).

siRNA transfections

The siRNA-based screens were performed by reverse transfection of U-2 OS cells cultured in CELLSTAR 96-well-plates (Greiner Bio-One) for 72 hr at a cell density of 4000 cells per well at the time of transfection with Ambion Silencer Select siRNAs at a final concentration of 5 nM using HiPerFect (QIAGEN) reagent. Individual siRNA transfections were performed for 72 hr with Ambion Silencer Select siRNAs using Lipofectamine RNAiMAX (Thermo Fisher Scientific). The following Silencer Select siRNAs were used in individual assays: siWDR33 (s30772/#1, s30771/#2, s30773/#3; unless stated otherwise s30772/#1 was used), siCPSF30 (s21412), siCPSF160 (s26658), siFIP1 (s37692), siCDC45 (s15831), siBRCA2 (s2085), siRPA1 (142498), siTHOC1 (s19395/#2), siTHOC2 (s32861/#1 and s32862/#2), siENY2 (s32449), siTPR (s14353), and siNUP153 (s19374). A second siRNA against THOC1 (#1) was from QIAGEN. Additional siRNAs against WDR33 were from Sigma-Aldrich (HU-11890-1) and QIAGEN (HS_WDR33_5). For individual siRNA transfections all siRNAs were used at a final concentration of 25 nM unless stated otherwise. When several siRNAs were combined, the final siRNA concentration was identical for all conditions within one experiment. Negative Silencer Select controls Neg1 and Neg2 from Ambion were used as non-targeting controls and are abbreviated "siCon." The siWDR33 RC phenotype and its rescue by THOC1 co-depletion were additionally confirmed using QIAGEN and Microsynth negative control siRNAs. All siRNA IDs are provided in the Key Resources Table.

Immunostaining

Cells were grown on sterile 12 mm glass coverslips, fixed in 3% formaldehyde in PBS for 15 min at room temperature, washed once in PBS, permeabilized for 5 min at room temperature in PBS supplemented with 0.2% Triton X-100 (Sigma-Aldrich), and washed twice in PBS. Where indicated, cells were pre-extracted in ice-cold PBS/0.2% Triton X-100 for 2 min on ice prior to formaldehyde fixation to measure detergent-resistant, chromatin-bound protein levels. All primary antibodies (see below for specifications) and secondary antibodies (Alexa fluorophores, Life Technologies) were diluted in filtered DMEM containing 10% FBS and 0.02% Sodium Azide.

Antibody incubations were performed for 1-2 hr at room temperature. Following antibody incubations, coverslips were washed once with PBS and incubated for 10 min with PBS containing 4',6-Diamidino-2-Phenylindole Dihydrochloride (DAPI, 0.5 μg/mL) at room temperature to stain DNA. Following three washing steps in PBS, coverslips were briefly washed with distilled water and mounted on 5 μL Mowiol-based mounting media (Mowiol 4.88 (Calbiochem) in Glycerol/TRIS). When immunostaining was combined with DNA-FISH all steps were performed as above except that cells were permeabilized for 5 min with 0.5% Triton X-100 (Sigma-Aldrich) on ice and all primary antibodies (see below for specifications) and secondary antibodies (Alexa fluorophores, Life Technologies) were diluted in 2% BSA. For detection of RNA:DNA-hybrids by the S9.6 antibody cells were fixed in ice-cold 99% methanol for 10 min at −20°C, washed three times in PBS and blocked in 2% BSA in PBS for 1 hr at room temperature. Antibodies were diluted in PBS supplemented with 2% BSA, and primary antibody incubations were performed overnight at 4°C, followed by a 1 hr secondary antibody incubation at room temperature. The following primary antibodies were used for immunostaining: H2AX Phospho S139 (mouse, Biolegend 613401, 1:1000), Cyclin A (rabbit, Santa Cruz sc-751, 1:100), Cyclin A (mouse, Abcam ab16726, 1:100) RPA70 (rabbit, Abcam ab79398, 1:500), BrdU (1:100, B44, 347580; BD), S9.6 (mouse, Kerafast ENH001, 1:200), 53BP1 (rabbit, Santa-Cruz sc-22760, 1:500), RPA32 Phospho S4/8 (rabbit, Bethyl A300-245A, 1:500), RPA32 (mouse, Abcam ab2175, 1:500), LaminB1 (rabbit, Abcam ab16048, 1:900).

DNA-FISH

After incubation with secondary antibodies following the immunostaining protocol, samples were fixed again in 3% formaldehyde for 10 min. Cells were washed twice for 5 min in 2X SSC (SSC: 150 mM NaCl, 15 mM sodium citrate) and subsequently incubated with hybridization buffer (50% formamide, 2X SSC, 1 mg/mL BSA, 1 mg/mL yeast tRNA (Thermo Fisher Scientific, 15401011), 10% dextran sulfate) for 1 hr at 37°C. After the pre-hybridization step cells were hybridized for 10 min at 80°C with Cy3 labeled DNA probe detecting the lac operator array diluted in hybridization buffer at a final concentration of 100 nM and incubated overnight at 37°C. The day after hybridization coverslips were washed with 2X SSC, 1X SSC and 0.5X SSC three times each for 5 minutes at 37°C, and incubated for 10 min with 0.5X SSC containing DAPI (0.5 μg/mL) at room temperature min stain DNA. Following two washing steps in 0.5X SSC and a final wash in PBS, coverslips were briefly washed with distilled water and mounted on 5 μL Mowiol-based mounting media (Mowiol 4.88 (Calbiochem) in Glycerol/TRIS).

RNA-FISH

For poly(A) RNA-FISH, samples were washed once in PBS and fixed in 3% formaldehyde for 10 min. Upon fixation samples were washed once in PBS and permeabilized for 5 min on ice with 0.5% Triton X-100 in 1X PBS. Samples were incubated 5 min in 1xPBS followed by 5 min in 2X SSC and subsequently incubated with hybridization buffer (50% formamide, 2X SSC, 1 mg/mL BSA, 1 mg/mL yeast tRNA (Thermo Fisher Scientific), 10% dextran sulfate) for 1 hr at 37°C. After the pre-hybridization step cells were hybridized overnight at 37°C in hybridization buffer containing Cy3-oligo(dT)40 at a final concentration of 100 nM. The day after hybridization coverslips were washed with 2X SSC, 1X SSC and 0.5X SSC three times each for 5 min at 37°C, and incubated for 10 min with 0.5X SSC containing DAPI (0.5 μg/mL) at room temperature to stain DNA. Following two washing steps in 0.5X SSC and a final wash in PBS, coverslips were briefly washed with distilled water and mounted on 5 μL Mowiol-based mounting media (Mowiol 4.88 (Calbiochem) in Glycerol/TRIS). ACTB RNA-FISH was performed using Stellaris DesignReady FISH Probes: Human ACTB with Quasar 670 Dye and Human ACTB intron with Quasar 570 Dye according to the manufacturer's protocol. Following the final washing step, coverslips were briefly washed with distilled water and mounted on 5 μL Mowiol-based mounting media (Mowiol 4.88 (Calbiochem) in Glycerol/TRIS). RNA-FISH samples were visualized on a Leica DMI 6000 inverted microscope using an HCX Plan APO DIC 63x oil objective (1.4-0.6 NA) and analyzed using Fiji.

DNA fiber analysis

Following the depletion of proteins of interest, cells were sequentially pulse-labeled with 30 μM CldU (Sigma-Aldrich) and 250 μM IdU (European Pharmacopoeia) for 20 min each. The cells were collected and resuspended in PBS at 2.5×10^5 cells per mL. The labeled cells were diluted 1:1 (v/v) with unlabeled cells, and 3 μL of cells were mixed with 7 μL of lysis buffer (200 mM Tris-HCl (pH 7.5), 50 mM EDTA, and 0.5% (w/v) SDS) on a glass slide. After 9 min, the slides were tilted to 15-45°, and the resulting DNA spreads were air-dried and fixed in methanol/acetic acid (3:1) solution overnight at 4°C. The DNA fibers were denatured with 2.5 M HCl for 90 min, washed several times with PBS to neutralize the pH and blocked with 0.1% Tween 20 in 2% BSA/PBS for 40 min. The newly replicated CldU and IdU tracks were labeled for 2.5 hr in the dark, at room temperature, with anti-BrdU antibodies recognizing CldU (rat, Abcam ab6326, 1:500) and IdU (mouse, BD 347580 B44, 1:100), followed by 1 hr incubation with secondary antibodies at room temperature in the dark: anti–mouse Alexa Fluor 488 (1:300, A11001, Invitrogen) and anti-rat Cy3 (1:150, 712-166-153, Jackson ImmunoResearch Laboratories). Fibers were visualized on a Leica DMI 6000 inverted microscope using an HCX Plan APO DIC 63x oil objective (1.4-0.6 NA) and analyzed using Fiji. At least 100 fibers were analyzed per replicate condition. Results are depicted as median whisker plots (5%–95% percentile).

Quantitative image-based cytometry (QIBC)

Automated multichannel wide-field microscopy for quantitative image-based cytometry (QIBC) for the initial screens was performed on an ImageXpress micro system equipped with IR-laser hardware autofocus and a Photometrics CoolSNAP HQ digital CCD camera (1392 × 1040 pixels, pixel size 6.45 μm x 6.45 μm, 12-bit dynamics). All other QIBC experiments were performed on an Olympus ScanR Screening System equipped with an inverted motorized Olympus IX83 microscope, a motorized stage, IR-laser hardware autofocus, a fast emission filter wheel with single band emission filters, and a 12bit digital monochrome Hamamatsu ORCA-FLASH 4.0 V2 sCMOS camera (2048 × 2048 pixel, pixel size 6.5 μm x 6.5 μm, 12 bit dynamics) as described previously (Michelena et al., 2018). For each condition, image information of large cohorts of cells (typically at least 500 cells for the UPLSAPO 40x objective (NA 0.9), at least 2000 cells for the UPLSAPO 20x objective (NA 0.75), and at least 5000 cells for the UPLSAPO 10x (NA 0.4) and UPLSAPO 4x (NA 0.16) objectives) was acquired under non-saturating conditions. Identical settings were applied to all samples within one experiment. Images were analyzed with the Olympus ScanR Image Analysis Software version 3.0.0, a dynamic background correction was applied, nuclei segmentation was performed using an integrated intensity-based object detection module using the DAPI signal, and foci segmentation was performed using an integrated spot-detection module. All downstream analyses were focused on properly detected interphase nuclei containing a 2C-4C DNA content as measured by total and mean DAPI intensities. Fluorescence intensities were quantified and are depicted as arbitrary units. Color-coded scatterplots of asynchronous cell populations were generated with Spotfire data visualization software version 7.0.1 (TIBCO). Within one experiment, similar cell numbers were compared for the different conditions. For visualizing discrete data in scatterplots, mild jittering (random displacement of data points along the discrete data axes) was applied in order to demerge overlapping data points. Representative scatterplots and quantifications of independent experiments, typically containing several thousand cells each, are shown. Representative images, in which the individual color channels have been adjusted for brightness and contrast, accompany selected quantifications. For the initial screen, the percentage of cells in RC was determined for each well based on chromatin-bound RPA and γH2AX formation upon HU plus ATRi treatment. RC was defined as the cellular state in which the soluble RPA pool was exhausted (cells show maximal RPA loaded onto the chromatin) and ATR-independent γH2AX formation can be observed (Toledo et al., 2013). The percentage of cells in RC was used to calculate a z-score ($z = (x - \mu) / \sigma$ with x being the percentage of cells in RC, μ being the mean of the percentage of cells in RC across all wells, and σ being the standard deviation of the percentage of cells in RC across all wells) to rank wells according to their replication stress sensitivity.

Confocal microscopy

Confocal images were acquired on an automated Leica SP5 inverted confocal laser scanning microscope equipped with diode, argon, and helium neon lasers (405 nm, 488 nm, 561 nm, 633 nm) using an HCX PL APO Leica 63x immersion oil objective (NA 1.4). RPA foci co-localization with the nuclear lamina was quantified from 3D z stacks.

Chromatin fractionation

Cell pellets were collected by scraping in 1x PBS supplemented with 1x protease inhibitor cocktail (cOmplete, Roche) and split in two equal fractions: (A) for the total proteome, cells were resuspended in 1x MNase buffer (0.3 M Sucrose, 50 mM Tris pH 7.5, 30 mM KCl, 7.5 mM NaCl, 4 mM $MgCl_2$, 1 mM $CaCl_2$, 0.125% NP-40, 0.25% Na-Deoxycholate) supplemented with 1x protease inhibitor cocktail and 10 U of MNase for every 5 million cells. Cells were incubated for 30 min at 37°C, boiled in 1x SDS-loading buffer for 5 min, spun down at 16000 x g for 5 min and the supernatant was collected for immunochemical assays. (B) For chromatin-bound and soluble fractions, cells were resuspended in chromatin extraction buffer (10 mM HEPES pH 7.6, 3 mM $MgCl_2$, 0.5% Triton X-100, 1 mM DTT) supplemented with 1x protease inhibitor cocktail. Cells were rotated for 30 min at room temperature and spun down at 1300 x g for 10 min at 4°C. The pellet was kept and the supernatant was centrifuged at 16000 x g for 5 min at 4°C and collected again (soluble fraction). It was boiled in 1x SDS-loading buffer for 5 min, spun down at 16000 x g for 5 min and used for immunochemical assays. The pellet of the chromatin extraction step (chromatin-bound fraction) was resuspended in MNase buffer supplemented with 1x protease inhibitor cocktail and 10 U of MNase for every 5 million cells. Cells were incubated for 30 min at 37°C, boiled in 1x SDS-loading buffer for 5 min, spun down at 16000 x g for 5 min and the supernatant was collected for immunochemical assays. Protein amounts were quantified using the standard Bradford method before addition of the SDS-PAGE loading buffer.

Immunochemical methods

Proteins were resolved by SDS-polyacrylamide gel electrophoresis (SDS-PAGE) and transferred onto polyvinylidene fluoride (PVDF) membranes. Membranes were blocked with PBS-Tween20 (0.01%) containing 5% milk powder for 1 hr at room temperature. Primary antibodies in blocking solution were applied over night at 4°C. The following primary antibodies were used for western blot analysis: Histone H3 (rabbit, Abcam ab1791, 1:50000), CHK1 Phospho S317 (rabbit, Cell Signaling 2344, 1:500), CHK1 Phospho S345 (rabbit, Cell Signaling 2348, 1:500), RNA Pol II (mouse, Active Motif 39097, 1:5000), RNA Pol II pS2 CTD (rabbit, Abcam ab5095, 1:5000), WDR33 (rabbit, Novus Biologicals NB100-58831, 1:500), THOC1 (mouse, Santa-Cruz sc-136426, 1:1000), RPA32 Phospho S4/8 (rabbit, Bethyl A300-245A, 1:500), RPA32 (mouse, Abcam ab2175, 1:500), Aquarius (rabbit, ProteinTech 243421-AP, 1:1000), Tubulin (mouse, Sigma T6199, 1:2000), KAP1 phospho S824 (rabbit, Abcam ab70369, 1:500), KAP1 (rabbit, Bethyl A300-274A, 1:1000), PCNA (mouse, Santa-Cruz sc-56, 1:2000), GAPDH (mouse, Merck MAB374, 1:50000), GFP (rabbit, Torrey Pines Biolabs TP401,

1:2000). Secondary horseradish peroxidase-coupled antibodies (Vector labs & Thermo Fisher Scientific) were applied for 1 hr at room temperature in PBS-Tween20 (0.01%) containing 1% milk powder prior to detection by ECL-based chemiluminescence.

Chromatin immunoprecipitation (ChIP)

For cross-linking and chromatin extraction, 3×10^7 cells were fixed for 8 min with 1% formaldehyde at room temperature followed by quenching with glycine (final concentration 0.12 M) and incubation for 10 min on ice. Cells were harvested and incubated for 10 min in 5 mL 10 mM EDTA, 10 mM TRIS (pH 8.0), 0.5 mM EGTA on ice, followed by centrifugation at 680 x g for 5 min. Cells were resuspended in 5 mL buffer containing 0.25% Triton X-100, 1 mM EDTA, 10 mM TRIS, 0.5 mM EGTA, and 200 mM NaCl and incubated for 10 min on ice followed by centrifugation at 680 x g for 5 min. Final cell lysis was performed with 20 mM TRIS (pH 8.0), 5 mM $MgCl_2$, 1 mM $CaCl_2$, 10 mM NaCl, 0.25 M Sucrose, and 1% Triton X-100 in a total volume of 0.9 mL on ice. Chromatin was fragmented with 40 Units S7 nuclease per 1.5×10^7 cells for 15 min at 37°C and the reaction was stopped with 500 mM NaCl, 20 mM EDTA, 10 mM EGTA, and 0.1% SDS. Fragmented chromatin was subjected to three sonication cycles (30 s ON / 30 s OFF) in a Bioruptor Pico instrument (Diagenode), centrifuged at 12000 x g for 10 min at 4°C, and the supernatant was used for further steps. 50 μL Dynabeads Protein A/G magnetic beads per IP were preblocked for 1 hr at 4°C in 1 x TRIS/EDTA with 100 ng tRNA and 10 μg/mL BSA, supplemented with 1 x protease inhibitor cocktail mix (PIC), and taken up in 50 μL 1 x TE with 1 x PIC per IP. Chromatin was incubated with 20 μL blocked beads for 1 hr at 4°C for pre-clearing. After bead removal, 5% input material was saved and 100 μg chromatin was incubated with 5 μg of phosphoserine-2 RNA Pol II antibody rotating overnight at 4°C. Immunoprecipitation was performed with 30 μL of blocked Protein A/G beads for 3h at 4°C. Beads were washed under rotation for 8 min per each wash step and placed on a magnetic rack for 2 min for exchange of buffers first with two rounds of high salt buffer (50 mM HEPES, 1 mM EDTA, 1% Triton X-100, 0.1% deoxycholate, 0.1% SDS, and 500 mM NaCl), one round of DOC buffer (250 mM LiCl, 0.5% NP-40, 0.5% deoxycholate, 1 mM EDTA, 10 mM TRIS), and two rounds of 1 x TRIS/EDTA buffer. Beads and input chromatin were treated with 60 μg RNaseA for 30 min at 37°C in 1% SDS, 0.1 M $NaHCO_3$, and subsequently 60 μg proteinase K for 3 h at 55°C in 1% SDS, 0.1 M $NaHCO_3$, 10 mM EDTA, 20 mM TRIS, followed by de-crosslinking overnight at 65°C. DNA was purified using QIAGEN MinElute PCR Purification Kit for IP samples and NucleoSpin PCR Clean-up for input, according to the manufacturer's instructions, and was eluted in 20 μL and 40 μL EB, respectively.

ChIP-sequencing and read processing

For ChIP-seq, libraries were prepared using the NEB-next ChIP-seq library Kit following the standard protocols. Individual samples with different index barcodes were combined at equal molar ratios and sequenced as pools. Sequencing of library pools was performed on Illumina HiSeq 4000 machines according to Illumina standards, with 125-bp single-end sequencing. Library demultiplexing was performed following Illumina standards. Samples were filtered for low-quality reads and adaptor sequences using Trim Galore. Reads mapped to the human genome (version hg38) using QuasR in R, allowing for two mismatches and only unique mapping reads were used. PCR duplicates were removed. Wiggle tracks were extracted using QuasR directly from bam files and visualized using the UCSC genome browser. Raw sequencing files and wiggle tracks have been uploaded to GEO under the accession number: GSE118795

Genomic coordinates and analysis at active genes

Genomic annotations are based on the *Homo sapiens* assembly version GRCh38/hg39 from December 2013. Human transcript coordinates were obtained from the RefSeq gene predictions at NCBI (Annotation Release: GCF_000001405.37_GRCh38.p11, 2017-12-22). To reduce redundancy due to too many transcripts per gene, we have retained only the longest annotated transcript per gene and have calculated the size of each individual gene based on their genomic coordinates using the GenomicRanges package in R. For downstream analysis we focused only on active genes, which were selected based on the phosphoserine-2 RNA Pol 2 signals in the siControl sample. We selected genes with an average log2FC over 0.5 in both replicates over the corresponding input. Log2FC for each gene was calculated as following: 1) first read counts per gene were normalized to gene length; 2) enrichment was calculated using the following formula: log2(IP_reads+8)-log2(Input_reads+8). For the representation in Figure 6B we have calculated the fold change of IP over input in 3000 bins per gene, including x 1/10 of gene length upstream and x 1 full gene length downstream. For heatmap representation and clustering, we have further removed all active genes shorter than 1300 nt to avoid interference with the Pol2 signal at promoter sites.

RNA extraction and quantitative PCR (qPCR)

RNA was purified with TRIzol reagent (Life Technologies). RNA was primed with random hexamers (Roche) and reverse-transcribed to cDNA using a MultiScribe Reverse Transcriptase (Thermo Fisher). Relative transcription levels were determined by normalizing to GAPDH and RPS21 as indicated. qPCR was performed with KAPA SYBR FAST qPCR Kit (KAPA Biosystems) on a Rotor-Gene Q system (QIAGEN). Samples were run in duplicates or quadruplicates and results are depicted as relative fold changes. All primer sequences are provided in the Key Resources Table.

Clonogenic survival assays

U-2 OS cells were seeded at single cell density and exposed to HU or ATRi for 24 hr. All conditions were performed in triplicates. Cells were then incubated for 10 days and the number of colonies with more than 50 cells was counted after staining with crystal violet (0.5% crystal violet in 20% ethanol).

Co-immunoprecipitation

To enrich endogenous WDR33 for analysis of interacting proteins of the CPSF complex, whole cell lysates were collected in RIPA buffer (50 mM Tris pH 8, 150 mM NaCl, 1% Igepal CA-630, 0.1% SDS, 0.1% Na-deoxycholic acid) supplemented with 2 mM $MgCl_2$, Benzonase (1:10000, Merck), 1x protease inhibitor cocktail (cOmplete, Roche) and 1x phosphatase inhibitor cocktail (PhosSTOP, Roche) and sonicated three times using a Branson Sonifier Cell Disruptor B15 (pulsed mode, output control 3, duty cycle 50%). The lysates were then diluted in an equal volume of 50 mM Tris pH 8 containing 50 mM NaCl and cleared by centrifugation for 30 min at 15000 x g and 4°C. 10% of the volume was kept for input controls. Upon antibody addition (WDR33, Novus Biologicals NB100-58831, 1:500; IgG, Santa-Cruz sc-2027, 1:500), samples were rotated for 2 hr at 4°C. 50 μL of equilibrated beads (Protein G Sepharose 4 Fast Flow, GE) were added and the samples were rotated for another 2 hr at 4°C. The beads were then collected by centrifugation at 1000 x g for 5 min at 4°C and washed three times in RIPA buffer prior to SDS-PAGE using a Bolt 4%–12% Bis-Tris Plus Gel (ThermoFisher) in Bolt MOPS SDS running buffer (ThermoFisher). The gel was stained with InstantBlue (Sigma) for 15 min at room temperature and washed 3 times with distilled water prior to band excision for mass spectrometry.

Mass spectrometry

Whole gel lanes from IP-WDR33 and IP-IgG samples were separated into six molecular weight sections. Each section was cut in small pieces and washed twice with 100 μL 100 mM NH_4HCO_3 / 50% acetonitrile, followed by a wash with 50 μL acetonitrile. The supernatants were discarded and 20 μL trypsin (5 ng/μl in 10 mM Tris / 2 mM $CaCl_2$, pH 8.2) plus 40 μL buffer (10 mM Tris/ 2 mM $CaCl_2$, pH 8.2) were added. Samples were heated in a microwave oven for 30 min at 5W and 60°C (Discover System, CEM). The supernatants were removed and the gel pieces extracted with 150 μL 0.1% TFA / 50% acetonitrile. The extracts were dried, dissolved in 20 μL 0.1% formic acid and transferred to autosampler vials for LC/MS/MS. Aliquots of 6 μL were analyzed on a nanoAcquity UPLC (Waters Inc.) connected to a Q Exactive mass spectrometer (Thermo Scientific) equipped with a Digital Pico-View source (New Objective). Peptides were trapped on a Symmetry C18 trap column (5 μm, 180 μm x 20 mm, Waters Inc.) and separated on a BEH300 C18 column (1.7 μm, 75 μm x 150 m, Waters Inc.) at a flow rate of 250 nl/min using a gradient from 1% solvent B (0.1% formic acid in acetonitrile, Romil) / 99% solvent A (0.1% formic acid in water, Romil) to 40% solvent B / 60% solvent A within 60 min. Mass spectrometer settings were: Data dependent analysis. Precursor scan range 350 – 1500 m/z, resolution 70'000, maximum injection time 100ms, threshold 3e6. Fragment ion scan range 200 – 2000 m/z, Resolution 35'000, maximum injection time 120ms, threshold 1e5. Proteins were identified using the Mascot search engine (Matrix Science, version 2.5.1.3). Mascot was set up to search the SwissProt database (release 2016_06) assuming trypsin digestion. Mascot was searched with a fragment ion mass tolerance of 0.030 Da and a parent ion tolerance of 10.0 PPM. Oxidation of methionine was specified in Mascot as a variable modification. Scaffold (Proteome Software, version 4.8.7) was used to validate MS/MS based peptide and protein identifications. Peptide identifications were accepted if they achieved a false discovery rate (FDR) of less than 0.1% by the Scaffold Local FDR algorithm. Protein identifications were accepted if they achieved an FDR of less than 1.0% and contained at least two identified peptides. Each gel section was analyzed individually and search results of the sections of each gel lane were merged in Scaffold.

QUANTIFICATION AND STATISTICAL ANALYSIS

For QIBC analysis, between 4 and 100 images per condition, depending on the microscope objective used and the cell confluence (i.e., 4 images with a 4x objective to obtain images of up to 5000 cells at a resolution sufficient to score RC; 100 images with a 40x objective to score re-localization of nascent transcripts and genomic loci), were acquired in an unbiased fashion from asynchronous cell populations grown on glass coverslips or multi-well plates. Typically between 2000 and 5000 cells per condition were analyzed, and representative single cell data of cell cohorts of comparable size are shown as two-dimensional cell cycle-resolved scatterplots. In Figures S4A and S4B averages ± SD are also indicated. In Figures S5A, S5B, S5I, and S6B median boxplots plus outliers are shown. For DNA fiber length measurements, at least 100 fibers were scored for each condition from n = 2-3 independent experiments, and the results are depicted as median plus 5-95 percentile whisker plots. Unpaired t test was used for statistical analysis. Replication initiation events were scored from at least 100 fibers per condition from n = 2-3 independent experiments and the results are depicted as means ± SD. Individual data points are shown in the same graphs and unpaired t test was used for statistical analysis. To score distances from the nuclear periphery, at least 150 events per condition were analyzed from n = 2-3 independent experiments, and scatterplots plus means are provided. Mann-Whitney test was used for statistical analysis. Percentages of cells with the MS2 focus at the nuclear periphery, or with pRPA S4/8 at the LacO array, were obtained from triplicates and means ± SD are shown. Individual data points are provided in the same graphs and unpaired t test was used for statistical analysis. Percentages of cells with RPA foci at the nuclear periphery were obtained from confocal z stacks of between 30 and 70 cells per condition and are depicted as means ± SD. Individual data points are provided in the same graphs and Mann-Whitney test was used for statistical analysis. Clonogenic survival assays quantification was performed in triplicates from n = 2-3 independent experiments, means ± SD

are shown, and unpaired t test was used for statistical analysis. Micronuclei were quantified from n = 4 independent experiments and means ± SD are shown. qPCRs to confirm knockdown efficiencies were performed in technical duplicates or quadruplicates, and the results are depicted as means ± SD, individual data points are provided in the same graphs. GraphPad Prism Version 7.0 was used for all statistical analyses and $p \geq 0.05$ was considered not significant (N.S.).

DATA AND SOFTWARE AVAILABILITY

The accession number for the RNA Pol II pS2 ChIP-seq data reported in this paper is GEO: GSE118795

Additional unprocessed datasets have been deposited on Mendeley: https://doi.org/10.17632/3p6bvgb5ys.1